Tomographic Reconstruction of Vector Fields in the Presence of Noise

Zachary Kemp

Student No. 20780370

`zachary.kemp@monash.edu`

November 4, 2011

Supervisors: Michael Morgan & David Paganin

Acknowledgements

Declaration of Originality

I, Zachary Kemp, hereby declare that this thesis and the work presented herein is entirely my own work. Where results from the work of others is used in any way, full acknowledgement to the sources is provided. No part of this thesis has previously been submitted for any other degree at this, or any other, institution.

Abstract

Vector field electron tomography (VFET) is the reconstruction of a vector field (the vector potential) from its projections. This requires phase contrast techniques, the acquisition of at least two tilt-series, and a tomographic reconstruction algorithm. In the present work, tomographic reconstructions were performed on simulated tilt series data for a transmission electron microscope. By varying defocus and noise level over successive simulations, power law relationships between optimum defocus and noise level, and minimum error and noise level, were found. Optimum values for the regularisation parameter used to stabilise the phase retrieval algorithm were obtained. The resolution of the method was also investigated, with reconstruction error curves presented as a function of separation distance for two dipoles. This work will facilitate improvements in the characterisation of magnetic nano-materials, enabling improvements in their design.

Contents

1   Introduction to Tomography

Tomography is the reconstruction of three-dimensional object functions from recorded two-dimensional projections. Tomographic reconstruction techniques can be employed to produce images of *microscopic* objects using, for example, synchrotron radiation [1] and electron microscopy [2]. The three-dimensional structure of *macroscopic* objects can also be probed using these techniques, as is routinely done in x-ray computed tomography (CT) used for medical imaging. The technique has been extended to the three-dimensional imaging of binary stars using Doppler measurements [3]. In recent decades, the process of tomographic reconstruction has been applied to the imaging of vector fields [4–6]. The methods discussed in this thesis utilise a transmission electron microscope (TEM) to probe magnetic materials, and rely on phase contrast to reconstruct the magnetic vector potential..

The essence of tomography is embodied in the Fourier slice theorem [7], which shows that the Fourier transform of a one-dimensional projection of a two-dimensional object function is equivalent to a one-dimensional slice through the origin of the two-dimensional Fourier transform of the object function. The two-dimensional Fourier transform of a function, $f(x, y)$, is given by [8:330]:

$$\tilde{f}(k_x, k_y) = \int \int f(x, y) e^{-2\pi i (k_x x + k_y y)} \, \mathrm{d}x \, \mathrm{d}y, \tag{1}$$

where k_x and k_y are the Cartesian reciprocal space coordinates corresponding to the real space coordinates x and y, respectively. Setting k_y equal to zero produces a slice, S_1, through the origin in reciprocal space:

$$S_1 = \int \int f(x, y) e^{-2\pi i k_x x} \, \mathrm{d}x \, \mathrm{d}y \tag{2}$$

$$= \int \left[\int f(x, y) \, \mathrm{d}y \right] e^{-2\pi i k_x x} \, \mathrm{d}x. \tag{3}$$

The term in brackets is the projection, P_1, of $f(x, y)$ onto the x-axis, and Eq. (3) is the Fourier transform of P_1. Extending this to three dimensions provides a relationship between the two-dimensional projection of the function, and a two-dimensional slice of the Fourier transform of the function. The three-dimensional Fourier transform of a function, $f(x, y, z)$, is given by [8:340]:

$$\tilde{f}(k_x, k_y, k_z) = \int \int \int f(x, y, z) e^{-2\pi i (k_x x + k_y y + k_z z)} \, \mathrm{d}x \, \mathrm{d}y \, \mathrm{d}z, \tag{4}$$

where k_z is the reciprocal space coordinate corresponding to the real space coordinate z. The two-dimensional slice, S_2, through the origin at $k_z = 0$ is:

$$S_2 = \int \int \int f(x, y, z) e^{-2\pi i(k_x x + k_y y)} \, \mathrm{d}x \, \mathrm{d}y \, \mathrm{d}z \tag{5}$$

$$= \int \int \left[\int f(x, y, z) \, \mathrm{d}z \right] e^{-2\pi i(k_x x + k_y y)} \, \mathrm{d}x \, \mathrm{d}y. \tag{6}$$

The term in brackets is the projection, P_2, of $f(x, y, z)$ onto the xy plane, and Eq. (6) is the two-dimensional Fourier transform of P_2. This is the form of the Fourier slice theorem that is used in three-dimensional tomography, in which a series of projections (tilt series) is used to produce the three-dimensional Fourier transform of the function, which is then inverse Fourier transformed to recover the complete three-dimensional function in real space. This is shown schematically in figure 1.

Vector tomography is an extension of these principles. The aim is to reconstruct a vector field, rather than a scalar distribution, from projections of the field. Due to the three degrees of freedom in a vector field, at least two orthogonal tilt series and an external boundary condition must be used to obtain all three components of the vector field [6], [9]. Typically, in the reconstruction of the magnetic vector potential, the external boundary condition used is the Coulomb gauge condition $\nabla \cdot \mathbf{A} = 0$. The addition of the gradient of a scalar function to the vector potential leaves the magnetic field unchanged, a property known as gauge invariance. Thus, a condition such as the above choice of gauge is required to determine the vector potential uniquely. An example of a possible geometry for the acquisition of multiple tilt series is shown in figure 2 [9].

Early applications of vector tomography involved the reconstruction of the velocity field of fluid flows from time of flight measurements of acoustic signals [4] and Doppler shift ultrasound [5]. More recently, these techniques have been applied to the reconstruction of magnetic vector potentials at the nanoscale [6]. An electron beam traversing a scalar and/or vector potential acquires a phase shift due to the Aharonov-Bohm effect (this point is discussed in more detail in section 3.2). Information about the electromagnetic properties of a sample can be inferred from the phase of the electron beam downstream from the sample. The charge-coupled device (CCD) detector in the TEM is sensitive only to the intensity of the electron beam and cannot measure the phase of the wavefunction. In order to determine the phase, an interferometric technique, or alternatively a through-focal phase retrieval method can be used. Each method has advantages and disadvantages. These are discussed further in section 3.2.

In the following sections, the theoretical basis of VFET, as well as the experimental application of the techniques, is described. The effects of noise on tomographic reconstructions of vector potentials are discussed, and the results of simulations, which offer insight into the noise-robustness of the algorithms, are presented. Due to the vast volume of research in the literature relating to scalar tomography, the focus here will be almost exclusively on the reconstruction of vector fields (specifically the magnetic vector potential) of which there is comparatively very little work reported in the literature. However, the electric potential is also an intrinsic aspect of the electromagnetic properties of a material, and will be discussed briefly in the context of separating the electric and magnetic phase shifts (section 3.3).
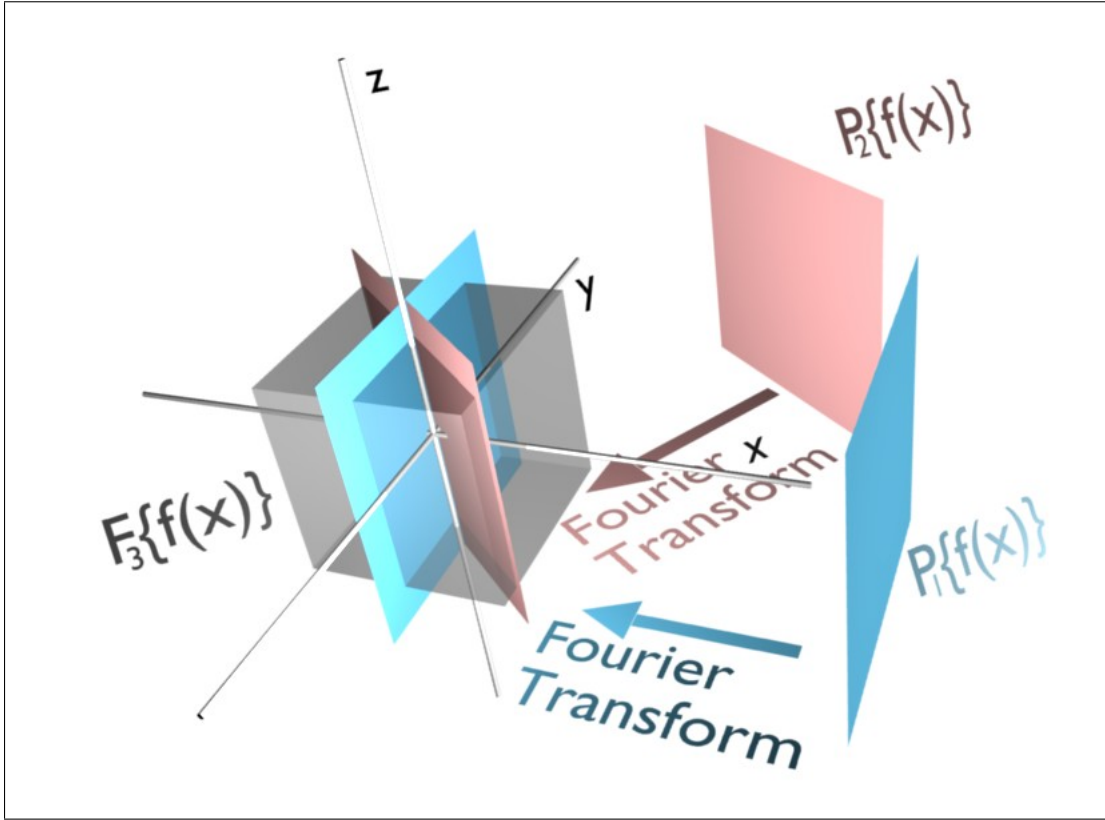
Figure 1: Schematic explanation of the Fourier slice theorem, showing the relationship between two projections P_1 (cyan) and P_2 (pink) of the object function $f(\mathbf{x})$, and the Fourier transform $\mathcal{F}_3\{f(\mathbf{x})\}$ (gray). The coloured squares on the right represent two projections in a tilt series about the z-axis. The coloured squares *inside* the box represent the two-dimensional Fourier transforms of the respective projections or, equivalently, slices through the origin of the three-dimensional Fourier transform of the object function, parallel to the projections.

2 Motivation for Vector Field Electron Tomography (VFET)

Tomography has many applications. Scalar tomography has become an indispensable diagnostic tool in the field of medical imaging in the form of CT scanning [10:1], positron emission tomography, and magnetic resonance imaging. Vector tomography has been used to image the velocity field of fluid flows in a medical imaging [5], as well as in an oceanographic [11], context. With the advent of the nanotechnology industry, and the explosion of research into the engineering of nanomaterials, comes the need to be able to characterise the magnetic properties of these materials [12]. Transmission electron microscopy has provided a means to investigate the structural properties of materials at the nanoscale, but has not been capable of fully characterising the magnetic properties of these materials. The use of vector tomography to image the magnetic properties of nanomaterials is relatively new, and further research into the techniques and their applicability to various geometries will enable improved characterisation of these materials which will, in turn, enable improvements in their design.

Examples of structures with magnetic properties at the nanoscale, and therefore potential applications for VFET, include: spintronics devices; magnetic semiconductor nanostructures [13]; magnetotactic bacteria [14], magnetic fluorescent nanospheres [15], and magnetic nanomotors [16]. The engineering of devices, such as high density magnetic hard disk drives and mag-
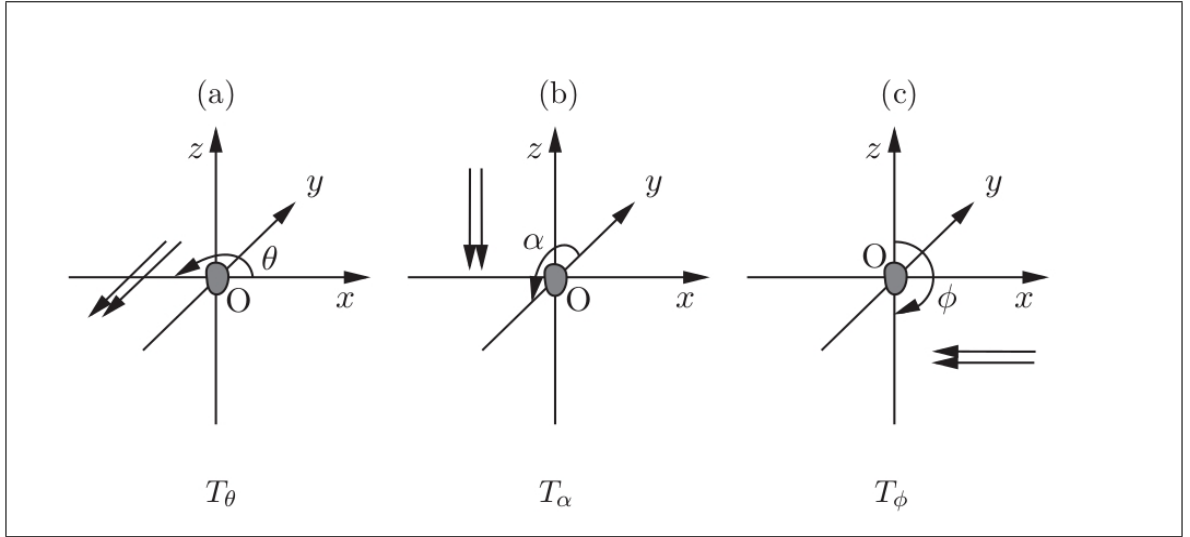
Figure 2: Example of three orthogonal tilt series: (a) T_θ, where the rotation is performed about the z-axis and the incident electrons travel in the $-y$ direction; (b) T_α, where the rotation is performed about the x-axis and the incident electrons travel in the $-z$ direction; and (c) T_ϕ, where the rotation is performed about the y-axis and the incident electrons travel in the $-x$ direction [9].

netic storage media, requires an understanding of their magnetic behaviour [17], [18], so the characterisation of the electromagnetic properties of these devices is another potential application. As the bit size of these devices continues to decrease, a corresponding increase in the resolution of techniques to characterise the properties is required. Nanostructured materials often exhibit novel physical properties not apparent in the bulk material [19], so methods capable of characterising these properties at the scale of interest are essential to understand their behaviour.

The experimental use of these vector tomography techniques is very much in its infancy, and a solid theoretical basis on which to design experiments and interpret the results is urgently required. In particular, an understanding of the sources of errors in the reconstruction will enable appropriate experimental controls to be implemented to produce more accurate reconstructions.

3 Methodology: Implementation of VFET

3.1 Overview

Tomography is the reconstruction of a three-dimensional object function from two-dimensional projections. The projections of a magnetic vector potential are given by line integrals (see Eq. 7 in section 3.2) which are proportional to the phase shift of the electron beam. After acquiring transmission electron micrographs of the sample, the first step in the reconstruction process is to convert the recorded intensities into phase distributions (discussed in section 3.2). The vector potential is then reconstructed from these projections using a suitable algorithm. These algorithms will be discussed in section 3.3.

3.2 Phase Retrieval

3.2.1 Introduction to Phase Retrieval for VFET

The interference of scattered electron waves produces features in the recorded TEM image due to differences in the phase of the interfering waves. This phenomenon is known as *phase contrast* [20:195]. In the present context, the phase contrast is due to the Aharonov-Bohm shift acquired by the electron beam as it traverses the sample, followed by the propagation of the resulting exit surface wavefield through the TEM imaging system. Under the projection approximation, the line integrals used to compute the phase shift at the exit plane are performed along straight lines in the direction of propagation. Phase contrast imaging is an essential aspect of the reconstruction of potentials using vector tomography, but its use poses the inherent difficulty of determining the phase based on intensity measurements. The spatial wavefunction, $\psi(\mathbf{r})$, associated with a monochromatic electron beam is a complex function of position, and can therefore be expressed as $\psi(\mathbf{r}) = |\psi(\mathbf{r})| \exp(i\varphi(\mathbf{r}))$, where $|\psi(\mathbf{r})|$ is the modulus of the wavefunction, and $\varphi(\mathbf{r})$ is the phase. Spin is ignored here, as the small scattering angles that occur in TEM imaging do not cause spin polarisation of electrons [20:20]. The detector in the TEM is sensitive only to the intensity, $|\psi(\mathbf{r})|^2$, of the electron beam, and not the phase. This means that the exit phase of the electron beam must be inferred from the measured intensity distribution rather than measured directly. This is known as the phase problem. Phase retrieval is the process of reconstructing $\varphi(\mathbf{r})$ based on measurements of $|\psi(\mathbf{r})|^2$.

In general, non-interferometric methods of phase retrieval require at least two intensity measurements in order to reconstruct the phase of the electron wave function [21]. For methods that rely on defocus, the measurements are taken in the form of a through-focal series, where intensities are recorded at various values of defocus. A through-focal series typically involves one measurement taken at the image plane, and one measurement either side of the image plane. These measurements represent 'slices' of the wavefunction at nearby planes orthogonal to the direction of propagation of the electron beam. This provides a finite difference approximation to the spatial derivative of the intensity along the direction of propagation of the electron beam, and from this can be obtained an expression for the phase. The specific method used will be discussed in section 3.2.2.

Interferometric methods require that the electron beam is split into two mutually coherent beams: a reference wave that propagates unimpeded, and an object wave, the phase of which is altered by the sample being probed [22]. Interference between the reference wave and the object wave provides a way to directly calculate the phase difference at a given position on the image plane from the measured intensity. Interferometry has the advantage of requiring only one image to be taken in order to determine the exit phase of the object wave and circumvents problems associated with taking out of focus images, but places coherence requirements on the beam that makes it unviable for many situations [22], provides a very limited field of view [23], and requires modifications to the TEM such as the addition of an electron beam splitter [24]. In addition to this, the phase solution is not unique for a given interference pattern due to the modulo 2π ambiguity of the phase. Because of this, phase unwrapping algorithms must be applied to the measured intensity to obtain the true phase [25].

If the sample is sufficiently thin and weakly interacting, it can be assumed that the *projection approximation* holds. The projection approximation treats the scattering as occurring at an "exit plane" immediately downstream from the sample. The electron rays are assumed to travel in straight, parallel lines through the sample. The projection approximation ignores the diffraction of the wavefunction as it traverses the scattering volume. This means that the phase of the electron beam at any pixel can be assumed to be a result of a shift acquired as it traveled

along a ray path through the sample. This produces a magnetic phase shift given by [26]

$$\varphi_m = -\frac{e}{\hbar} \int \mathbf{A} \cdot \hat{\mathbf{z}} \, \mathrm{d}z \tag{7}$$

in SI units - where e is the electron charge, $\hbar$ is the reduced Planck constant, c is the speed of light, $\mathbf{A}$ is the magnetic vector potential, and the integration is performed along a straight line path (under the projection approximation) in the z-direction - which is employed to infer the component of the vector potential in the direction of propagation of the electron beam. The wavefunction also acquires an additional phase shift due to the electric potential through which the beam passes. This is given by [26]

$$\varphi_e = \frac{e}{\hbar} \int V \mathrm{d}z \tag{8}$$

where V is the electric potential and the integration is performed along the electron's path over the direction of propagation z. This results in the total phase shift

$$\varphi = \varphi_m + \varphi_e$$
$$= \frac{e}{\hbar} \left(\int V \mathrm{d}z - \int \mathbf{A} \cdot \hat{\mathbf{z}} \, \mathrm{d}z \right). \tag{9}$$

In section 3.3, the process of disentangling these components to obtain the individual phase shifts is discussed. As an example of how these phase shifts can be used to reconstruct the potentials, the projection $T(x,z) = -\int \mathbf{A}_y(x,y,z)\mathrm{d}y$ of the vector potential $\mathbf{A}$ in the $-y$ direction is given in terms of the phase at the image plane by [9]

$$T(x,z) = -\frac{\hbar}{e}\varphi_m(x,z). \tag{10}$$

It is these components that are then used to reconstruct the three-dimensional vector potential after collecting numerous projections from at least two tilt series and applying a reconstruction algorithm (to be discussed further in section 3.3).

3.2.2   Transport of Intensity Equation

The transport of intensity equation (TIE) can be used to reconstruct the phase based on intensity measurements. The equation relates spatial derivatives of the intensity to the phase [27]:

$$-k\partial_z I(x,y,z) = \nabla_\perp \cdot (I(x,y,z)\nabla_\perp \varphi(x,y,z)). \tag{11}$$

Here $\nabla_\perp$ is the divergence operator acting in the (x,y) plane, k is the wavenumber of the electrons, $I(x,y,z)$ is the intensity, and $\varphi(x,y,z)$ is the phase. This expression assumes that the electron beam remains paraxial, and requires the intensity to be non-zero everywhere in the image-plane in order for a unique solution to exist [28], [29]. The TIE (11) suggests a finite difference approximation given by [30]:

$$-k\frac{I_+ - I_-}{2\Delta} \approx \nabla_\perp \cdot (I_0 \nabla_\perp \varphi(r_\perp)), \tag{12}$$

where Δ is the defocus distance, and the notation $\varphi(r_\perp) \equiv \varphi(x,y,z_0)$, $I_0 \equiv I(x,y,z_0)$, $I_+ \equiv I(x,y,z_0+\Delta)$, and $I_- \equiv I(x,y,z_0-\Delta)$, where $z = z_0$ is the image plane, has been introduced

for brevity. Inherent in this approximation is an error of $\mathcal{O}(\Delta^2)$, so its accuracy is improved by decreasing the defocus distance. The intensity is treated as though it changes linearly along the z direction. This is accurate when the defocus distance is small, but leads to artefacts in the reconstructed phase when the defocus distance is large. The reconstruction can be improved by using multiple defocused images in the reconstruction [31]. In addition to the errors caused by approximating the derivative via a first-order finite difference, this method results in a loss of spatial resolution due to defocus blurring [6].

Under the phase object approximation, the intensity is uniform across the image plane and Eq. (12) becomes

$$\nabla_\perp^2 \varphi(r_\perp) = -k\frac{I_+ - I_-}{2I_0\Delta}. \tag{13}$$

This can be solved using a Fourier transform method to give an expression for the phase [32:103-105]:

$$\varphi(r_\perp) = \frac{k}{I_0}\mathcal{F}^{-1}\frac{k_\perp^2}{k_\perp^4 + \alpha^4}\mathcal{F}\frac{I_+ - I_-}{2\Delta}, \tag{14}$$

where $k_\perp$ is the magnitude of the position vector in Fourier space and α is a positive, real parameter used to regularise the singularity at $k_\perp = 0$. The choice of the regularisation parameter, α, affects the accuracy of the algorithm, and the optimum value depends on other parameters such as noise and defocus. This point is explored in detail in section 6.5. Methods based on the TIE can be used when the Fresnel number,

$$N_F = a^2/\lambda\Delta, \tag{15}$$

where a is the characteristic transverse length scale of the electron wavefield at the exit surface of the sample and λ is the wavelength of the incident electron beam, is significantly greater than 1 [9].

Other through-focal phase retrieval methods exist as well as methods that employ image and diffraction plane pairs, but the work carried out for the current project used only the TIE method so the other methods will not be discussed here. For a description of some of these methods, see [33].

3.3   Reconstructing the Vector Potential

When the electron beam in a TEM passes through a magnetic vector potential $\mathbf{A}(\mathbf{r})$ and an electric scalar potential $V(\mathbf{r})$, the wave function acquires a phase shift φ due to the Aharonov-Bohm effect given by Eq. (9). The electric phase shift possesses time reversal symmetry, and the magnetic phase shift antisymmetry, meaning that the electric phase shift is unaltered, and the magnetic phase shift reversed, when the direction of propagation of the electron beam is reversed relative to the sample. Explicitly, the potentials transform under time-reversal such that [34:270-271]

$$V(\mathbf{x}, t) \to V_T(\mathbf{x}, t) = V(\mathbf{x}, -t) \tag{16}$$

and

$$\mathbf{A}(\mathbf{x}, t) \to \mathbf{A}_T(\mathbf{x}, t) = -\mathbf{A}(\mathbf{x}, -t) \tag{17}$$

where $V_T(\mathbf{x}, t)$ and $\mathbf{A}_T(\mathbf{x}, t)$ are the potentials under time reversal. This allows the two to be disentangled by first recording the forward phase shift φ_F, and then flipping the sample by 180° and recording the reversed phase shift φ_R. The magnetic and electric phase shifts are then given by [35]

$$\varphi_m = \frac{\varphi_F - \varphi_R}{2} \qquad (18)$$

and

$$\varphi_e = \frac{\varphi_F + \varphi_R}{2} \qquad (19)$$

respectively. These phase shifts can then be used separately to reconstruct the vector potential and scalar potential using vector tomography and conventional scalar tomography respectively.

The projections calculated from the retrieved phase shifts (see section 3.2) are used to construct the volumetric image of the potentials. There are various methods that can be employed to reconstruct the potentials. The Fourier slice theorem can be used to do this directly by way of *Fourier inversion*. The process involves reconstructing the reciprocal space potentials using the Fourier transformed projections, and then utilising a discrete inverse Fourier transform method to obtain the potentials in real space. The inversion can be achieved using the data from the transformed projections, but mapping the data to Cartesian coordinates using interpolation[1] allows the *Fast Fourier Transform* to be employed. This reduces the number of operations required to complete the reconstruction by a factor of $N^2 / \ln N$ [36:92-94]. Fourier inversion is computationally intensive and, in practice, is typically not used in the reconstruction process [7].

A numerically more practical approach is to use a *back-projection method* [7], where the projections are 'smeared' (back-projected) through the region of interest. Values are then assigned to each voxel based on the values of pixels in the projection. The contributions from each projection are then summed to obtain the final result. A simple diagram of the back-projection process is shown in figure 3. Unmodified, this back-projection method does not construct an accurate image of the object. Non-zero regions of the projection contribute to all parts of the reconstructed image along the back-projection path, leading to non-zero voxel values outside the object [10:176]. This effect can clearly be seen as gray regions in the right hand side of figure 3. The solution is to use a method known as *filtered back-projection* [10:179]. This method involves applying a high-pass filter to the projections. The resulting filtered projection can now contain negative valued pixels, so when the back-projections are summed, positive and negative values from respective filtered projections cancel out, resulting in a net contribution of zero to the voxels outside the object. A comparison between the unfiltered, and filtered, back-projection methods is shown in figure 4.

---

[1]The reciprocal space potentials are in polar coordinates because they are built up from slices through the origin rotated about the tilt angle.
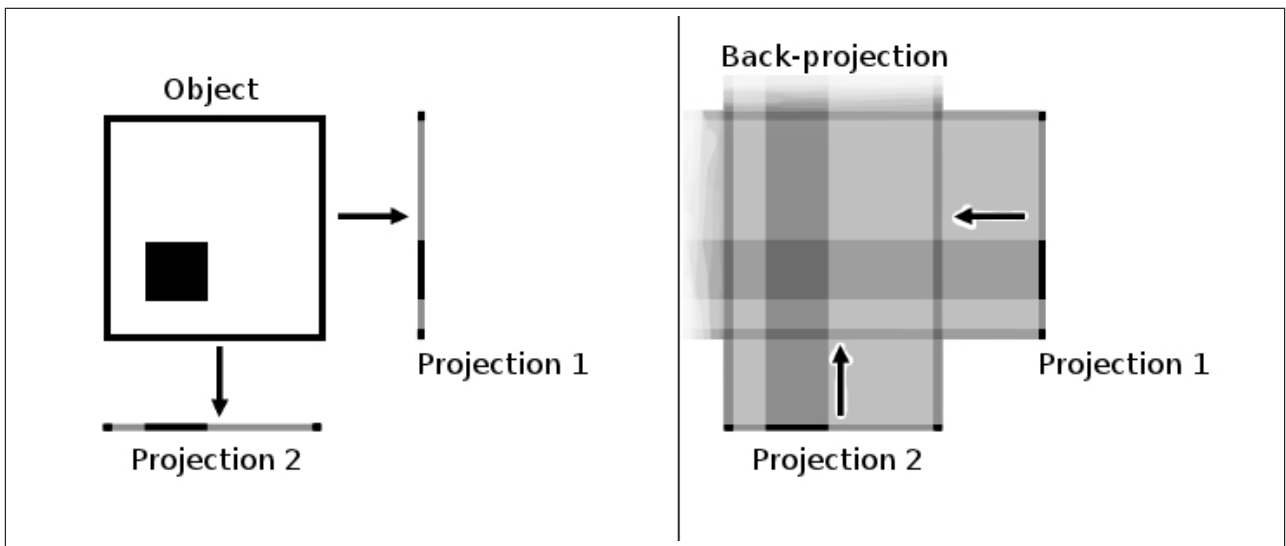
Figure 3: A two-dimensional object with two of its one-dimensional projections (left), and an approximation of the original object formed by back-projection (right). The result contains significant artefacts due to the small number of projections used in the reconstruction and the absence of high-pass filtering in the back-projection method used.
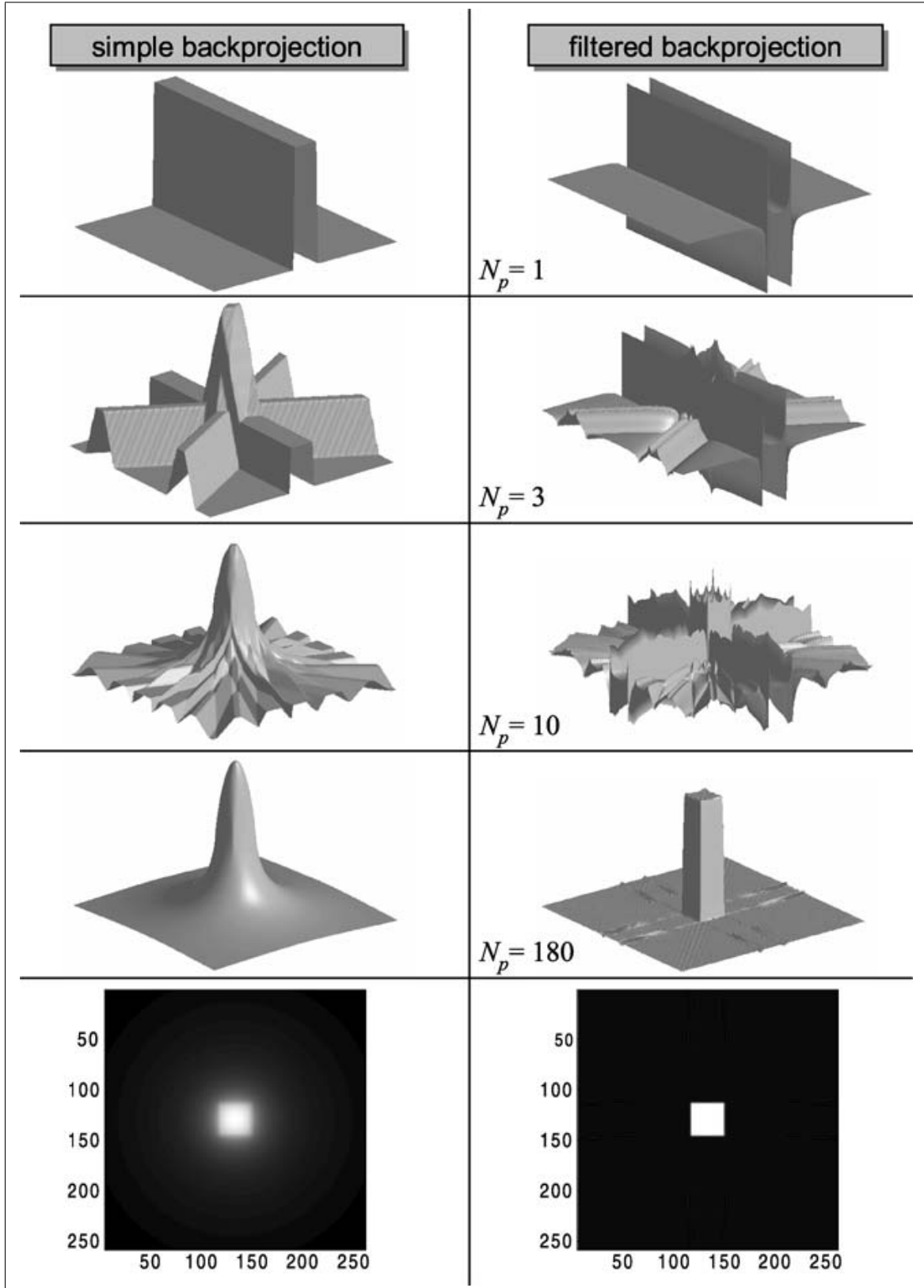
Figure 4: Comparison between unfiltered back-projection and filtered back-projection of a square for several numbers N_p of projections [10:185], clearly showing the superior result of filtered back-projection over unfiltered back-projection at $N_p = 180$.

15

4 Experimental Verification of the Effectiveness of VFET Techniques

The methods discussed in this report have been employed to measure and visualise the vector potential of a permalloy thin film [6]. A 27 nm thick, $1\times1\mu$m square sample was patterned using focused ion beam milling, resulting in electromagnetic properties that could be determined a priori, allowing the reconstructed vector potential to be compared against the theoretical [37:112-113]. Using a 200 kV electron beam, Phatak et al. [6] acquired micrographs in two orthogonal tilt series with a tilt increment of 2° over a range of ±70°. Each tilt angle consisted of one underfocus, one in focus, and one overfocus image with a defocus distance of 340 μm. The Coulomb gauge condition was applied to account for the third component of the vector potential. A TIE based algorithm was used to recover the phase shift, and time reversal symmetry was used to obtain the magnetic phase shift alone. The vector potential was then reconstructed via a filtered back-projection method.

The reconstructions of the magnetic field and vector potential are shown in figures 5 and 6 respectively. Figure 7 shows a comparison between the theoretical and experimental results. The main features of the magnetic structure, most notably the domain boundaries and the central vortex, can clearly be seen. Also apparent, however, are artefacts in the image, particularly near the edges of the structure. These artefacts are due to several factors. The limited tilt range of ±70° resulted in a missing wedge of information in each tilt series. This causes the elongation and blurring seen in the first two experimental results in figure 7. Defocus blurring and Fresnel fringes due to the use of out of focus images in the phase retrieval process also introduce errors in the reconstruction. Errors in the recovered magnetic phase shift arise due to misalignment of the sample after flipping when the total phase shifts in each direction are subtracted, and these contribute to the errors in the reconstructed potential. The experimental results show that the techniques discussed in this report constitute a viable method for visualising, in three dimensions, the vector potentials of magnetic nanostructures, but also highlight the need to characterise the causes of errors in the reconstructions, in order to minimise them in future applications.
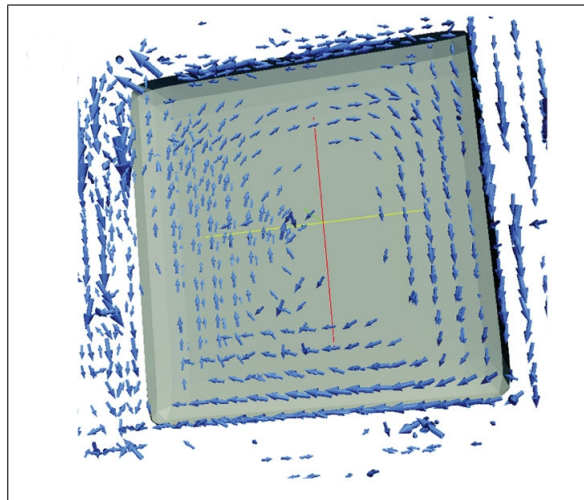

Figure 5: Reconstructed magnetic induction (blue arrows) around a 27 nm thick, $1 \times 1\mu$m square permalloy thin film [6].
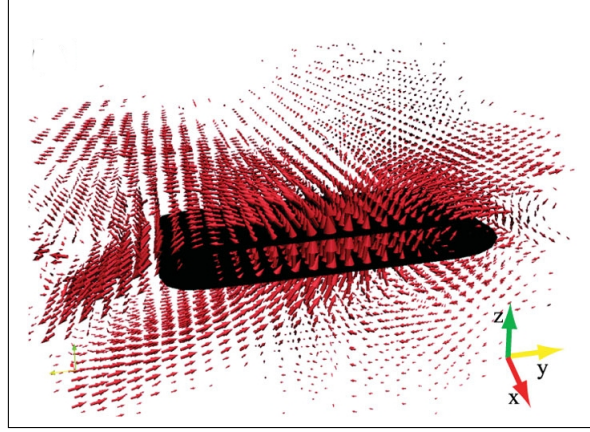
Figure 6: Reconstructed vector potential (red arrows) around a 27 nm thick, $1 \times 1\mu$m square permalloy thin film [6].
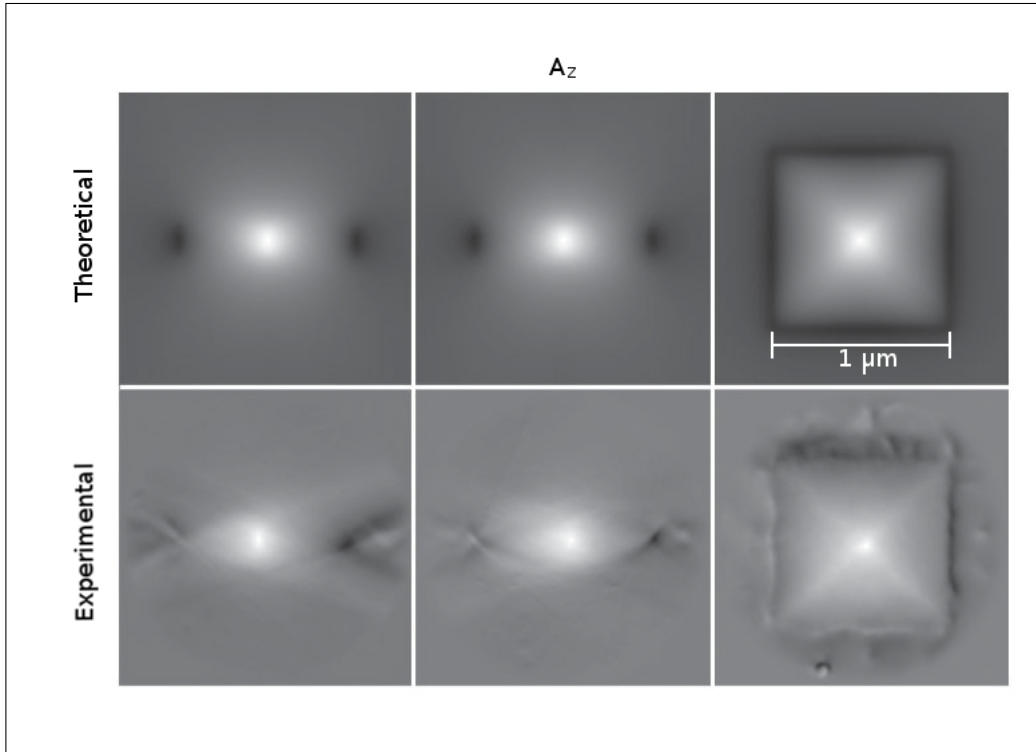
Figure 7: Comparison between the z component of the theoretical and experimental vector potentials of a 27 nm thick, 1×1 μm square permalloy thin film showing three orthogonal planes (xz, yz, and xy, respectively) through the origin. The experimental vector potential was reconstructed using two orthogonal tilt series with a tilt range of $\pm 70°$ and a sample flip to extract the magnetic component of the phase shift [6].

5 Characterisation and Effects of Noise

In practice, images acquired in the TEM contain both information about the object of interest (the *signal*), as well as unwanted *noise*. Yu et al. [9] have briefly investigated the effects of noisy data on the reconstructed vector potential for the simple case of a magnetic dipole. The analysis showed artefacts in the reconstructed image due to the occurrence of singular surfaces (to be discussed in section 5.2) in the reconstruction algorithm (See figure 8). The effects of noise on tomographic reconstructions has also been analysed by Lade et al. [38]. The algorithm (identical to that used by Yu et al. for the case shown on the left of figure 8) was found to be robust in the presence of noise, but produced an approximately constant normalised RMS error - defined below (Eq. (20)) - of ~10% for noise levels below about 2%. The cause of this error was considered to be due to singular surfaces in the reconstruction algorithm and the authors suggested regularisation or filtering as potentially viable methods for reducing this error. In a cubic voxel grid, this normalised RMS error is given by [9]:

$$E_{RMS} = \left\{ \frac{\sum_{ijk}^{M} |\mathbf{A}_{ret}(x_i, y_j, z_k) - \mathbf{A}_{ex}(x_i, y_j, z_k)|^2}{\sum_{ijk}^{M} |\mathbf{A}_{ex}|^2(x_i, y_j, z_k)} \right\}^{\frac{1}{2}}, \tag{20}$$

where $\mathbf{A}_{ret}$ and $\mathbf{A}_{ex}$ are the retrieved and exact vector potentials, respectively, the indices i, j, k are the indices of voxel locations, and M^3 is the total number of voxels.

The results from quantitative analyses of the effects of noise in imaging systems are important to ensure that the maximum possible amount of useful information can be obtained from the images. In the context of vector tomography, a thorough understanding of the effects of noise in the collected data is essential to enable the most appropriate reconstruction methods to be employed in a given application. For example, the relationship between error, defocus, and noise level, obtained using simulations (see section 6.1), provides a concrete way to minimise the errors by selecting a defocus distance. Or, if a particular defocus is required for a given application, a maximum allowable noise level can be found based on the maximum allowable error in the reconstruction. When the main source of noise is considered to be shot noise[2], the noise level can be decreased by increasing the image acquisition time. Shot noise follows a Poisson distribution [39:211], and the noise level is given by:

$$\sigma = 1/\sqrt{\langle n \rangle}, \tag{21}$$

where $\langle n \rangle$ is the mean number of photon counts per pixel [10:421]. This can be expressed in terms of acquisition time and probe current as [20:96]:

$$\sigma = \sqrt{\frac{e}{f I_P \tau}}, \tag{22}$$

where f is the fraction of electrons recorded by the detector, I_P is the probe current, and τ is the acquisition time for one image, divided by the number of pixels.

In conventional scalar tomography, the process of tomographic reconstruction results in the noise level being higher in the reconstructed image than in the projections [40:643-644]. However, in VFET, the reconstruction process applied to the retrieved phase maps has the effect of reducing errors due to noise rather than exacerbating them. This point is explored further in section 6.1.

---

[2]Shot noise is noise due to the random arrival, at the detector, of probe particles (in the case of VFET, electrons) due to the probabilistic nature of quantum mechanics.
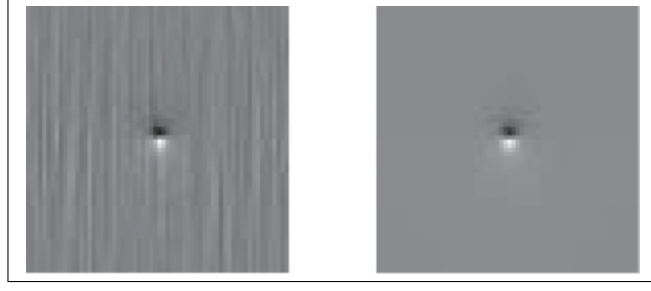
Figure 8: The x component of the reconstructed (left) and exact (right) vector potentials of a dipole, in a 128^3 voxel grid, plotted at $z = 0$ with 10% Gaussian noise [9].

5.1 Characterisation of Noise

Sources of noise in experimental data can be broadly classified into two categories: those of a stochastic nature, and those that are, to some extent, deterministic. In imaging systems, the former category includes shot noise, and thermal noise due to the random motion of conduction electrons within the detector. The latter category includes sinusoidal variations in the signal due to the unwanted presence of an electromagnetic signal caused by, for example, nearby wires carrying an alternating current. Noise of this type is predictable, and can be greatly reduced by characterising the effects of the noise and attempting to subtract it from the image. Stochastic noise, however, requires some form of averaging over neighbouring pixels in real space, or filtering of spatial frequencies in Fourier space, to be reduced. This inevitably leads to loss of information about the object being imaged. As an example, a low pass filter will leave only low frequency data in the image. If white noise is present in the image (white noise is equal in power in each spectral component over the entire frequency spectrum) a low pass filter can be used to remove frequencies above a cutoff frequency. The value of the cutoff frequency is chosen to reduce the amount of noise in the image, while minimising the loss of signal. If, however, there is significant high frequency data in the image, such as sharp edges, these will be smoothed along with the noise. The amount of smoothing will depend on the nature of the filter used, and a filter should be chosen such that the ratio of noise removed to image data lost is high. This particular method is not very effective in the context of tomographic reconstruction. This point will be explored in section 5.3.

5.2 Singularities in the Presence of Noise

The algorithms used in VFET can contain singularities. For example, consider the tilt series T_θ and T_α, where θ represents rotation about the z-axis with the electron beam propagating along the y-axis, and α is the rotation about the x-axis, with the electron beam propagating along the z-axis. Using these tilt series and the Coulomb gauge, $\mathbf{k} \cdot \tilde{\mathbf{A}} = 0$, the vector potential in reciprocal space can be reconstructed using the formulae: [9]

$$\tilde{A}_x = \frac{\tilde{T}_\theta k_r^\theta (k_y^2 + k_z^2) + \tilde{T}_\alpha k_r^\alpha k_x k_z}{k_y(k_x^2 + k_y^2 + k_z^2)}, \tag{23}$$

$$\tilde{A}_y = \frac{-\tilde{T}_\theta k_r^\theta k_x + \tilde{T}_\alpha k_r^\alpha k_z}{k_x^2 + k_y^2 + k_z^2}, \tag{24}$$

19

and

$$\tilde{A}_z = \frac{-\tilde{T}_\theta k_r^\theta k_x k_z - \tilde{T}_\alpha k_r^\alpha (k_x^2 + k_y^2)}{k_y(k_x^2 + k_y^2 + k_z^2)}, \tag{25}$$

where k_x, k_y, and k_z are the Cartesian reciprocal space coordinates, k_r^θ and k_r^α are the polar coordinates in terms of the radial component $r = \sqrt{x^2 + y^2 + z^2}$ and $\tilde{T}_\alpha$ and $\tilde{T}_\theta$ are the Fourier transformed tilt series corresponding to the tilt angles α and θ (see figure 2). It is apparent that $\tilde{A}_x$ and $\tilde{A}_z$ are singular at $k_y = 0$, and $\tilde{A}_y$ is singular at $k_x^2 + k_y^2 + k_z^2 = 0$. The singular surfaces at $k_y = 0$ are particularly problematic in the presence of noise. Small unwanted variations in intensity produce large deviations from the exact value for the components of the vector potential in reciprocal space. A simple example of the effect of noise at a singularity is shown in figure 9, where the function $f(k) = 1/k$ is plotted exactly and with white Gaussian noise added prior to dividing by k. For values of k far away from the singularity at $k = 0$, the curve obtained using noisy data is close to the exact curve, but as the curve approaches the singularity, the errors increase dramatically.
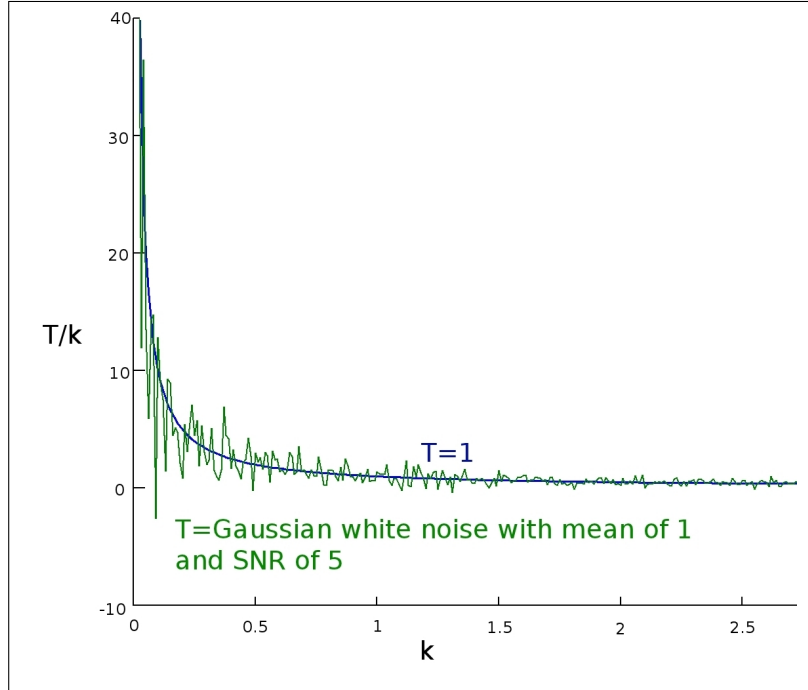

Figure 9: Example of a singularity in the presence of noise in one dimension. The function $f(k) = 1/k$ is plotted exactly (blue) and with 20% Gaussian noise added (green).

In the reconstruction formulae given by Eqs. (23)-(25) one component of the reciprocal space vector potential (in the above example $\tilde{A}_y$) contains a singular point at the origin, but no singular surface. If three orthogonal tilt series are acquired, three different sets of reconstruction formulae can be derived by choosing two of the tilt series and combining them with the divergenceless condition. Each set of formulae will have one component with no singular surface, and these can be combined to form a new set of formulae, thus avoiding singular surfaces in the reconstruction. Specifically, these formulae are [9]:

$$\tilde{A}_x = \frac{\tilde{T}_\theta k_r^\theta k_y - \tilde{T}_\phi k_r^\phi k_z}{k_x^2 + k_y^2 + k_z^2}, \tag{26}$$

$$\tilde{A}_y = \frac{-\tilde{T}_\theta k_r^\theta k_x + \tilde{T}_\alpha k_r^\alpha k_z}{k_x^2 + k_y^2 + k_z^2}, \tag{27}$$

and

$$\tilde{A}_z = \frac{-\tilde{T}_\alpha k_r^\alpha k_y + \tilde{T}_\phi k_r^\phi k_x}{k_x^2 + k_y^2 + k_z^2}, \tag{28}$$

where ϕ is the additional tilt angle, and $\tilde{T}_\phi$ its corresponding tilt series in Fourier space. Figure 2 shows the geometry used to acquire the third tilt series. Yu et al. [9] found that no streaking artefacts occurred when the vector potential was reconstructed in this way, suggesting that the artefacts were due to singular surfaces that exist in the filtered back-projection formulae using two tilt series. The acquisition of three orthogonal tilt series is not possible with current technology [9]. So, at present, minimising the impact that singular surfaces have on the reconstruction is essential for the accurate reconstruction of vector potentials.

5.3   Noise Reduction

The deleterious effects of noise can be partially overcome by implementing *noise-reduction algorithms*. There are numerous algorithms that can be used to reduce the amount of noise in an image, and the choice of algorithm depends on the nature of the noise and the image itself. White noise is an important consideration in imaging systems. Both thermal noise and shot noise can be closely approximated by white noise and in conventional x-ray CT, for example, the image quality is ultimately determined by the shot noise [41]. In two-dimensional images, averaging algorithms that smooth out the image in real space, and low pass filtering applied in Fourier space are most applicable for this type of noise [42]. Such algorithms typically involve applying a *mask*. Methods are then used to average pixels that fall within the mask (i.e. the neighbouring pixels), and the resultant value is taken as the new value for the given pixel. The smoothing can be linear in nature, or in the form of a weighted average of the pixel values within the mask. One of the drawbacks of such a method is that edges - regions where the intensity of the image varies greatly from pixel to pixel - are blurred along with the noise. The extent to which the signal is affected in this manner is dependent on the size of the mask, as well as the type of averaging used.

The technique of filtering requires modification in the present context. White noise, by definition, has equal power in all frequencies. To minimise noise in two-dimensional images, a low pass filter is often used to remove contributions above a certain frequency, thus removing much of the noise, but leaving the majority of the signal, which may not have much intensity in the higher frequencies, untouched. This type of technique is not as effective in the present context of phase retrieval and tomographic reconstruction. Consider the main contributors to errors in the reconstruction due to random noise. These are the singular surfaces discussed in section 5.2. In the example given, the singular surface occurs at $k_y = 0$. Removing frequencies above a certain value of k_y will not reduce the effect of these singular surfaces on the total error of the reconstruction. As this is the main contributor to the total error, the improvement will be minimal.

Figure 10(a) shows the effect of a low pass filter applied around $k = 2$, on the function plotted in figure 9. It is clear that such a method is ineffective at reducing errors when they are exacerbated by a singularity at the reciprocal space origin. While the low pass filter smooths the curve for high values of k, the noise in this region did not make a significant contribution to the error prior to filtering and the technique does nothing to reduce the large contribution to the error in the region around $k = 0$. One solution is to use a band-stop filter centred around the singularity. This will remove frequencies in the vicinity of the singular surfaces. Because

the noise in the data becomes more problematic closer to the singular surface, the removal of the frequencies should be complete at this value of k, and taper off as the distance from the singular surface increases. This will ensure that the significant effects of noise at, or near, the singular surfaces are avoided, while preventing unnecessary partial removal of the signal. The reason that the noise-reduction must be applied in a *smooth* fashion over the plane is that these singular surfaces occur in reciprocal space. Sharp features in reciprocal space, such as would occur due to rectangular spatial filtering, cause ringing artefacts in the real space image [43]. This effect, known as the Gibbs phenomenon, is undesirable and can cause the filter to actually contribute to the errors in the reconstruction. To filter out a specific range of spatial frequencies, a function can be multiplied by the acquired data in Fourier space to smoothly remove spatial frequencies at the singular surfaces. For example, the filter

$$\mathcal{N}(k_y) = \frac{k_y^2}{k_y^2 + w^2} \tag{29}$$

where w is the half-width at half maximum of the filter curve, is zero at the origin and approaches unity smoothly as the value of k_y increases. The effect of a filter of this form applied to a noisy signal at a singularity is shown in figure 10(b). Multiplying this function by the reciprocal space vector potential component $\tilde{A}_x$ (given by Eq. (23)) results in the modified component

$$\tilde{A}_{x(mod)} = \left(\frac{k_y^2}{k_y^2 + w^2} \right) \left(\frac{\tilde{T}_\theta k_r^\theta (k_y^2 + k_z^2) + \tilde{T}_\alpha k_r^\alpha k_x k_z}{k_y(k_x^2 + k_y^2 + k_z^2)} \right). \tag{30}$$

This modified component contains no singular surface, and this will affect the RMS error in the reconstruction. This method significantly reduces the wild variations in the reconstruction near the singularity, but has the disadvantage of causing the solution to deviate from the exact value in the region that the filter is applied[3]. Noise reduction algorithms have been effectively applied to data from conventional x-ray tomography [41], magnetic resonance imaging [44], and positron emission tomography [45], as well as scalar electron tomography [46]. The effect of filtering the noisy signal in this way has not been analysed for the case of vector tomographic reconstructions such as those given by Eqs. (23)-(25).

---

[3]This filtering is analogous to the regularisation of the TIE (Eq. (14)), though the form of the filter used here (Eq. (29)) is different to the filter, $\mathcal{N}(k_\perp) = \frac{k_\perp^4}{k_\perp^4 + \alpha^4}$, used for the TIE regularisation.
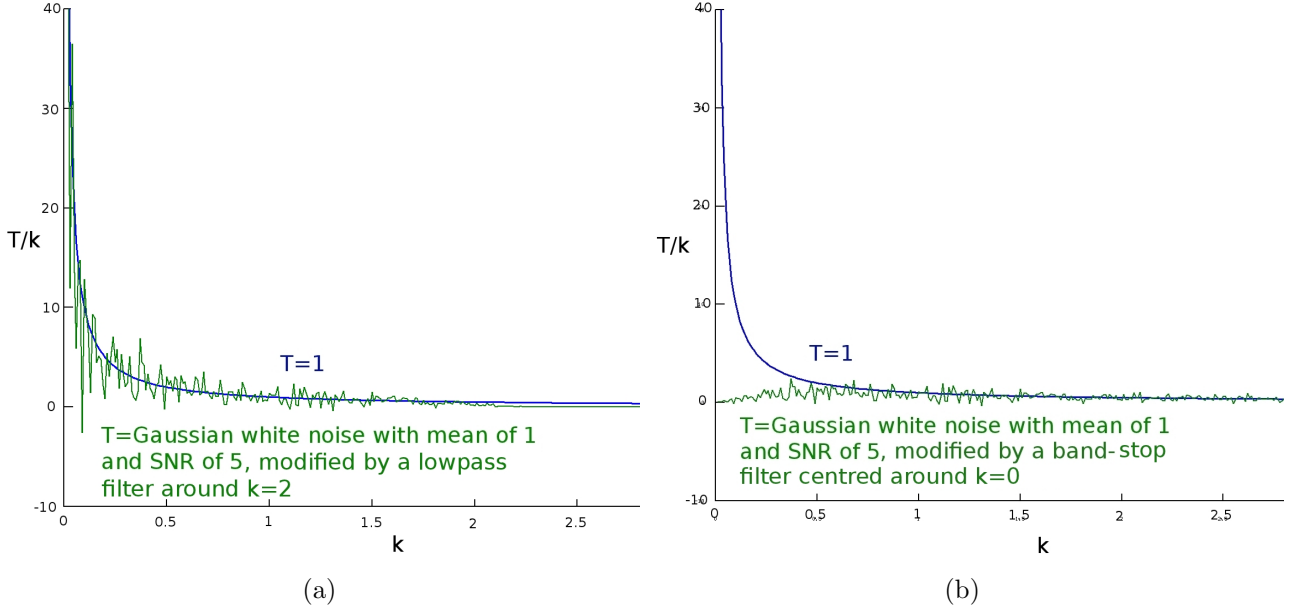
Figure 10: Effect of filtering on a singularity in the presence of noise. The function $f(k) = 1/k$ is plotted in each graph (blue). (a) The noisy signal from figure 9 modified by a low pass filter applied around $k = 2$, and (b) modified by a band-stop filter applied around $k = 0$.

5.4 Simulation of Poisson Noise

The noise considered in this project is shot noise. This type of noise follows a Poisson distribution [39:211]. The simulation of such noise involves conversion of the noise level, σ, to mean count number, $\langle n \rangle$, by Eq. (21). This count number is then adjusted to a mean *local* count number, $n(i,j)$, by multiplying by $I(i,j)/\langle I \rangle$, where $I(i,j)$ is the intensity of the pixel, and $\langle I \rangle$ is the mean intensity over the image. A new local count number $n_{noisy}(i,j)$ is then chosen from a Poisson distribution[4] with mean and variance of $n(i,j)$ (rounded to the nearest integer). Finally, the new local intensity is given by:

$$I_{noisy}(i,j) = \langle I \rangle \frac{n_{noisy}(i,j)}{\langle n \rangle}. \tag{31}$$

This method was used to simulate shot noise for the work described in the following section.

6 Results

6.1 Effects of Defocus on the RMS Error for a Dipole

The magnetic dipole is ubiquitous in nature because the fundamental building blocks of magnetic fields (the electron spin) are dipoles and any arbitrary field can be expressed as a superposition of dipoles. The vector potential of objects such as magnetic nanoshells, and the uniformly magnetised spheres discussed in section 6.4, is identical to that of a dipole outside the object. If a vector potential is expressed as an expansion of multipoles, the higher order multipole terms will die off more quickly with increasing distance than will the dipole term,

---

[4]For a numerical implementation, see Press et al. [47:294-295].

23

so the vector potential of any magnetic object will approximate a dipole at sufficiently large distances. For these reasons, the following work on the dipole vector potential in the context of VFET will be applicable to a wide range of geometries.

Tilt series simulations were carried out on a magnetic dipole, with the simulated micrographs used to compute the exit phase of the wavefunction, and a tomographic reconstruction algorithm applied to the phase maps to recover the vector potential. The form of the vector potential of a dipole oriented in the z-direction is [34:186]

$$\mathbf{A} = \frac{\mu}{r^3 + \delta^3} \begin{bmatrix} -y \\ x \\ 0 \end{bmatrix}, \tag{32}$$

where μ is the magnitude of the magnetic moment, $r = \sqrt{x^2 + y^2 + z^2}$ is the radial distance from the dipole, and δ is a regularisation parameter used to avoid the singularity at the origin.

A 300 kV paraxial electron wavefield incident on a magnetic dipole oriented in the z-direction was simulated. The dipole was located at the centre of a $(2^7)^3$ voxel grid, with the entire grid representing a 10^3 nm^3 region centred at the origin. A small but arbitrary value of δ such that $\delta^3 = 0.01$ nm^3 was chosen for the regularisation parameter. Electron micrographs for two orthogonal tilt series were simulated by computing the exit phase, $\psi(\mathbf{r})$, and calculating the wavefunction at the detector according to [48:590]:

$$\psi_{\pm\Delta}(\mathbf{r}) = \psi(\mathbf{r}) \otimes T_{\pm\Delta}(\mathbf{r}), \tag{33}$$

where $\psi_{\pm\Delta}(\mathbf{r})$ is the wavefunction at $z = z_0 \pm \Delta$, $\otimes$ is the convolution operator, and $T_{\pm\Delta}(\mathbf{r})$ is the transfer function. In Lorentz TEM image simulations, spherical aberration can be ignored [48:641], and the simulation does not involve attenuation, so the resulting transfer function is $T_{\pm\Delta}(\mathbf{r}) = \exp(\pm i\pi\Delta\lambda|\mathbf{r}|^2)$ [49:485]. The intensity at each defocus plane was then taken as the squared modulus of the wavefunction at the respective planes.

Each tilt series consisted of 100 tilt angles, with one overfocus and one underfocus micrograph recorded for each angle (computed by taking the square of the magnitude of the wavefield before and after the focal plane respectively). The in-focus intensity was assumed to be uniform because the effects of beam attenuation were not included in simulating the micrographs. A transport of intensity method (see section 3.2.2) was used to retrieve the phase of the wavefunction for each projection, and a filtered back-projection algorithm (section 3.3) was used to reconstruct the vector potential from the two tilt series and the Coulomb gauge condition. The resultant vector potential was compared against the vector potential computed directly from the dipole field within the voxel grid by calculating the normalised global RMS error as per Eq. (20).

Poisson noise was added to the each micrograph to simulate shot noise. The reconstruction was performed multiple times with the noise level in the simulated micrographs varying from 0% to 5% in increments of 0.5%, and $\mu\Delta$ (see footnote[5]) varying from 2 to 40 in units of $\frac{\hbar}{e} \times 10^6$ Am^3. A surface plot showing how the error in the reconstruction varies with defocus and noise is shown in figure 11. For high noise levels, the error suffers from a variability due to the random nature of the noise, evident as fluctuations in the surface plot. That is, the RMS error cannot be predicted exactly when the signal is noisy, but instead is distributed about some *mean*

---

[5]Under the phase object approximation, a change in Δ results in a change in measured intensity identical to that produced by a change in the magnitude of the vector potential by the same factor. Because the magnitude of the vector potential is proportional to μ, expressing the defocus in terms of $\mu\Delta$ generalises the results for any dipole moment.

theoretical value. This in turn affects the results for optimum defocus and minimum error. In order to significantly improve the smoothness of this plot, each point representing an error for a given noise level and defocus would need to be calculated multiple times and averaged over, providing a mean value of the RMS error for each point. Due to time constraints, this process was not carried out for this project.
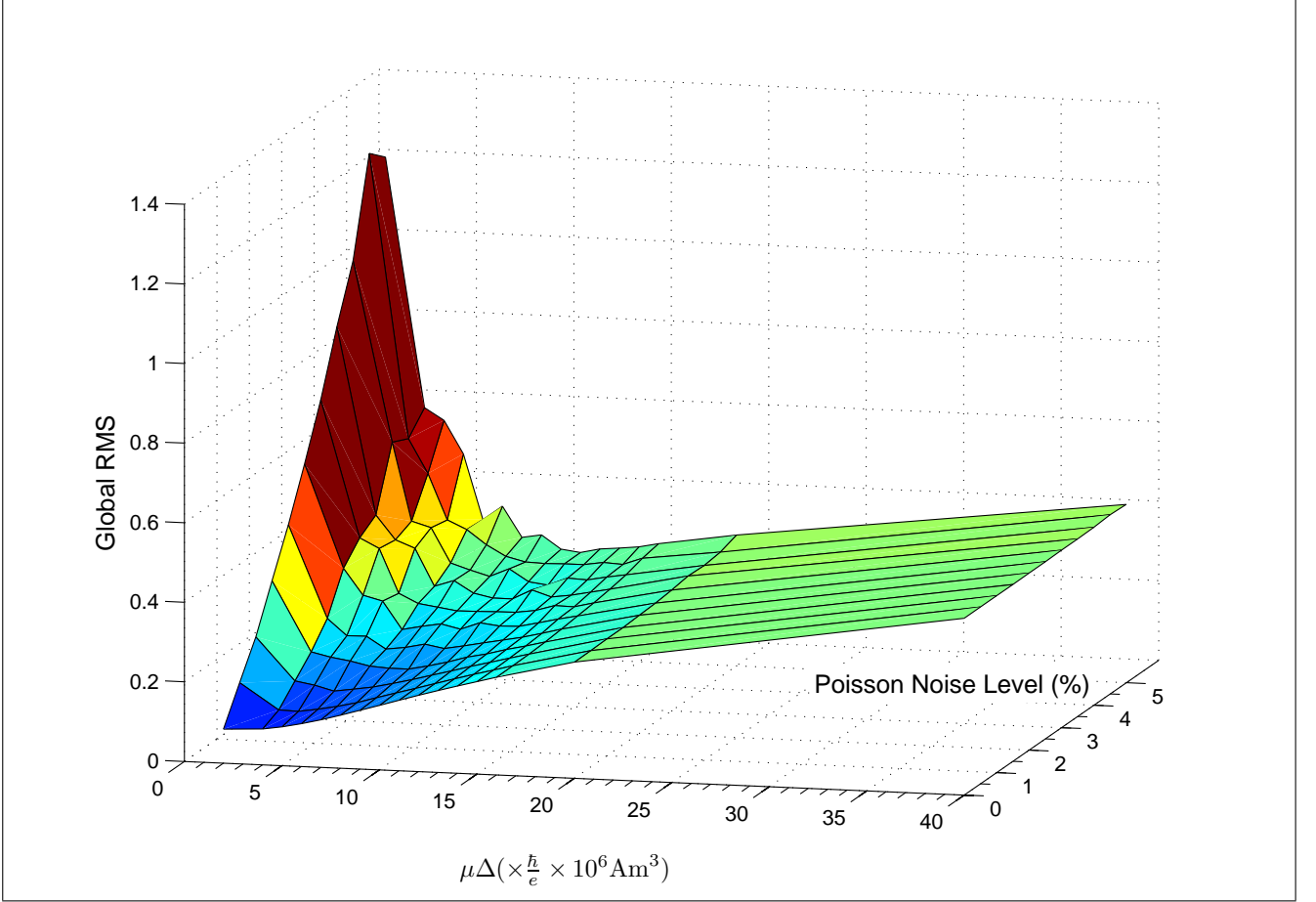

Figure 11: Plot of reconstruction error against noise level and the product of the magnitude μ of the magnetic moment and defocus Δ for a dipole centred at the origin.

It is evident that, for a given noise level σ, there exists a minimum error ($E_{\min}$) and a corresponding optimum defocus distance (Δ_{opt}). For a defocus distance shorter than this optimum, the signal intensity is small and the contribution from the noise becomes significant. For larger defocus, the errors in each phase map due to the finite difference approximation used to calculate the derivative dominate [50]. Thus, Δ_{opt} must be large enough that the signal rises significantly above the noise, but small enough that the finite difference approximation to the derivative is accurate.

It has been shown that, when using the TIE formalism, Δ_{opt} is proportional to $\sigma^{1/3}$ [50]. That is,

$$\Delta_{\mathrm{opt}} = A_1 \sigma^{1/3} \tag{34}$$

for some constant A_1. This analysis was performed by examining the error in the phase maps, so it does not take into account the effect that the tomographic reconstruction has on the relationship between Δ_{opt} and σ. Nevertheless, Eq. (34) offers a starting point from which the data can be analysed.

The smallest defocus used in the simulations was $\Delta = 5$ nm, but because the errors in the phase retrieval for small defocus are due to the effects of noise, for the noise-free case the theoretical Δ_{opt} is zero. Due to this, it can be assumed that the Δ_{opt} versus σ curve passes through the origin. Here, the assumed relationship (from Eq. (34)) is $\Delta_{\text{opt}} = A_1 \sigma^{p_1}$, where A_1 and p_1 are constants to be determined. From this, the linearised relationship

$$\ln(\Delta_{\text{opt}}) = p_1 \ln(\sigma) + \ln(A_1) \tag{35}$$

can be obtained. To the author's knowledge, no analysis of the relationship between E_{min} and noise analogous to the relationship between Δ_{opt} and noise discussed above has been performed. A logical approach here is to see if these data also fit a power law, although in this case the curve does not pass through the origin. The hypothesis that the minimum global RMS error (E_{min}) follows a curve of the form $E_{\text{min}} = A_2 \sigma^{p_2} + C$ for some numbers A_2, p_2, and C, implies the linear relationship

$$\ln(E_{\text{min}} - C) = p_2 \ln(\sigma) + \ln(A_2). \tag{36}$$

The number $C = 0.085$ is the y-intercept of the non-linearised curve. Because the value of E_{min} at this point corresponds to the case of zero noise, it was assumed to be a good approximation to the value of C and was used in the left hand side of Eq. (36) to obtain the linearised data. However, the value of C will be slightly overestimated using this method because Δ_{opt} for the noise-free case ($\Delta = 0$) cannot be used in practice. The value of $C = 0.085$ was taken as exact in computing $\ln(E_{min} - C)$ for each value of σ, which will contribute some uncertainty in the calculated values of p_2 and A_2.

Plots of $\ln(\Delta_{\text{opt}})$ against $\ln(\sigma)$ and $\ln(E_{\text{min}} - C)$ against $\ln(\sigma)$ are shown in figures 12(a) and 12(b), respectively. Linear regression was applied to the data for both plots to obtain the values $p_1 = 0.39 \pm 0.06$, $\ln(A_1) = 2.73 \pm 0.06$, $p_2 = 0.90 \pm 0.05$, and $\ln(A_2) = -3.2 \pm 0.05$. (The methods used to find the uncertainties in slope and intercept are given in Taylor [51:187-188]). The value of p_1 is consistent with the cube-root relationship of Eq. (34) within the calculated uncertainties. Applying these results to the original power laws, the equations are

$$\Delta_{\text{opt}} = (15.3 \pm 1) \times \sigma^{(0.39 \pm 0.006)} \tag{37}$$

and

$$E_{\text{min}} = (49 \pm 3) \times \sigma^{(0.90 \pm 0.05)} \times 10^{-3} + 0.085 \tag{38}$$
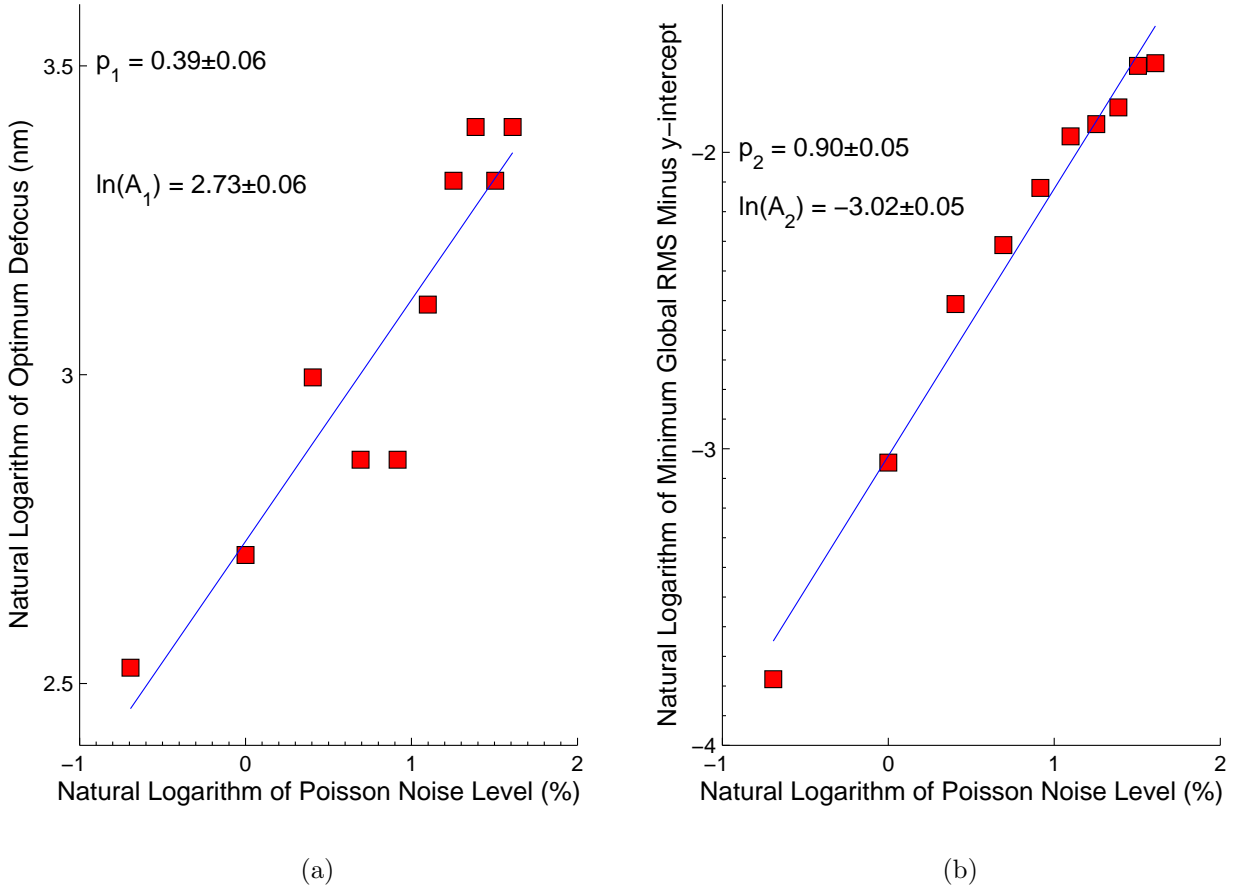
Figure 12: Properties of the reconstruction of the regularised dipole vector potential. (a) The natural logarithm of optimum defocus plotted against the natural logarithm of noise level. (b) The natural logarithm of the minimum error (minus the noise-free error) plotted against the natural logarithm of noise level.

Figure 13 shows projections of the exact and reconstructed vector potentials – and the retrieved phase – along each axis. The defocus and magnetic moment used gave $\mu\Delta = 2\frac{\hbar}{e} \times 10^6$ Am^3, with a noise level of 5%. The retrieved phase (second row) shows significant cloud-like artefacts due to the use of the transport of intensity method and the presence of noise in the micrographs. The form of these artefacts is caused by the transport of intensity equation (Eq. (14)) acting as a low pass filter with a sharp peak at the origin [52], exacerbating the effect of low frequency contributions to the noise while suppressing the high frequency contributions. When the noise considered is spatially uncorrelated white noise, as is the case in the current work, the contribution made by the noise in reciprocal space is independent of $k_\perp$. Thus, the noise is amplified near $k_\perp = 0$, and supressed at large $k_\perp$, by the $\frac{k_\perp^2}{k_\perp^4 + \alpha^4}$ term in Eq. (14) [50].

The cloud-like artefacts are largely absent in the reconstructed vector potential (third row), though other artefacts such as the horizontal banding in the x projection have appeared. Nevertheless, the dipole is clearly visible in the first two projections of the reconstructed vector potential. The normalised RMS error calculated in this case was 124%, illustrating the fact that qualitative features of the potentials can be very apparent, even when the RMS error is very high.
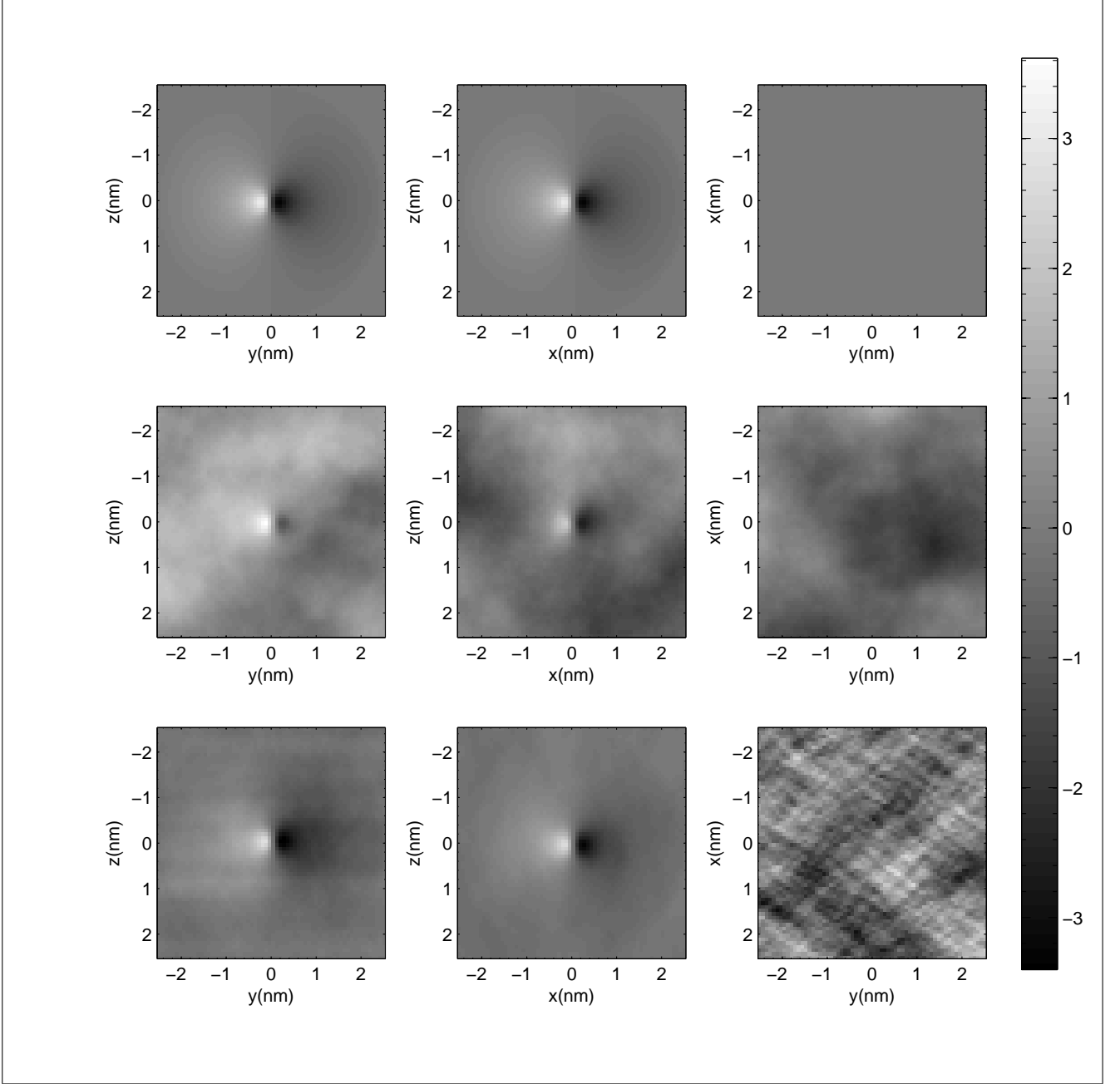
Figure 13: Projections of the simulated exact and reconstructed dipole vector potentials. Top row: Projections of exact vector potential. Middle row: phase maps reconstructed from the simulated micrographs. Bottom row: Projections of the vector potential reconstructed from the phase maps using filtered back-projection. Each dipole has magnetic moment μ, such that $\mu\Delta = 2 \times \frac{\hbar}{e} \times 10^6$ Am^3. The columns show projections in the x, y, and z directions, respectively. The normalised RMS error in the reconstruction of the vector potential for this case was 124%. The colour bar indicates the exit phase of the wavefunction in radians.

6.2   Spatial Resolution of the Tomographic Reconstruction

Spatial resolution is the ability of an instrument or technique to distinguish between two objects. In optics, the objects can be point sources, so the ability of the instrument to distinguish between two of these point sources will depend only on the distance between them, and the resolution can be defined as the minimum distance at which two point sources can be distinguished. Due to the fact that the magnetic dipoles considered here are not point-like objects, the resolution will depend on the magnitude of the magnetic moment because as this increases, the magnitude of the vector potential at a given distance from the dipole also increases. This causes a greater overlap in the vector potential of two adjacent dipoles, reducing the ability to distinguish between the two. In addition to this, the magnetic moment is a vector quantity, so it has a direction as well as a magnitude. Because of these considerations, the ability of a vector tomography algorithm to resolve detail will depend on the strength and relative orientation of the constituent magnetic moments.

In order to investigate the resolving capability of these methods, tilt series were simulated for two dipoles. All parameters - magnetic moments, grid size, voxel number, regularisation parameters and orientation - were the same as those used in section 6.1. Two identical dipoles separated by a distance d in the x-direction were simulated for both the parallel and antiparallel case. The exact, and reconstructed, projected potentials, and the retrieved phase maps, are shown in figure 14. Figures 15 and 16 show plots of the RMS error versus separation distance (d) for parallel and antiparallel dipoles with $\mu\Delta = 7.91 \times 10^{-6}$ Am^3 and $\mu\Delta = 2.85 \times 10^{-6}$ Am^3, respectively, with each calculated for the noise-free case and the case of 4% noise. For the case of parallel dipoles, the reconstruction is stable in the presence of noise. The addition of 4% Poisson noise in the micrographs increases the error by a few percent at most, with the greatest effect occuring for large d. This is because, when d is small, the potentials sum to produce a net potential with a high magnitude. This in turn increases the phase shift, and hence the signal, at the detector leading to a diminished effect due to the noise. For the case of *antiparallel* dipoles, the opposite is true. When d is small, the potentials sum to produce a net potential with a small magnitude, resulting in a decrease in the phase shift at the detector. This causes the noise to have a significant impact when the seperation distance is small, with significant implications regarding the resolving capability of this method at, for example, magnetic domain boundaries.

The resolution of the reconstruction will depend on how much error is considered acceptable. For example, if a normalised RMS error of 30% is deemed to be the maximum acceptable error in a particular application of VFET, then one could not expect to resolve detail on a scale smaller than about 1.5 Å in an array of dipoles, each with magnetic moment $\mu = 7.91\Delta^{-1} \times 10^{-6}$ Am^3.
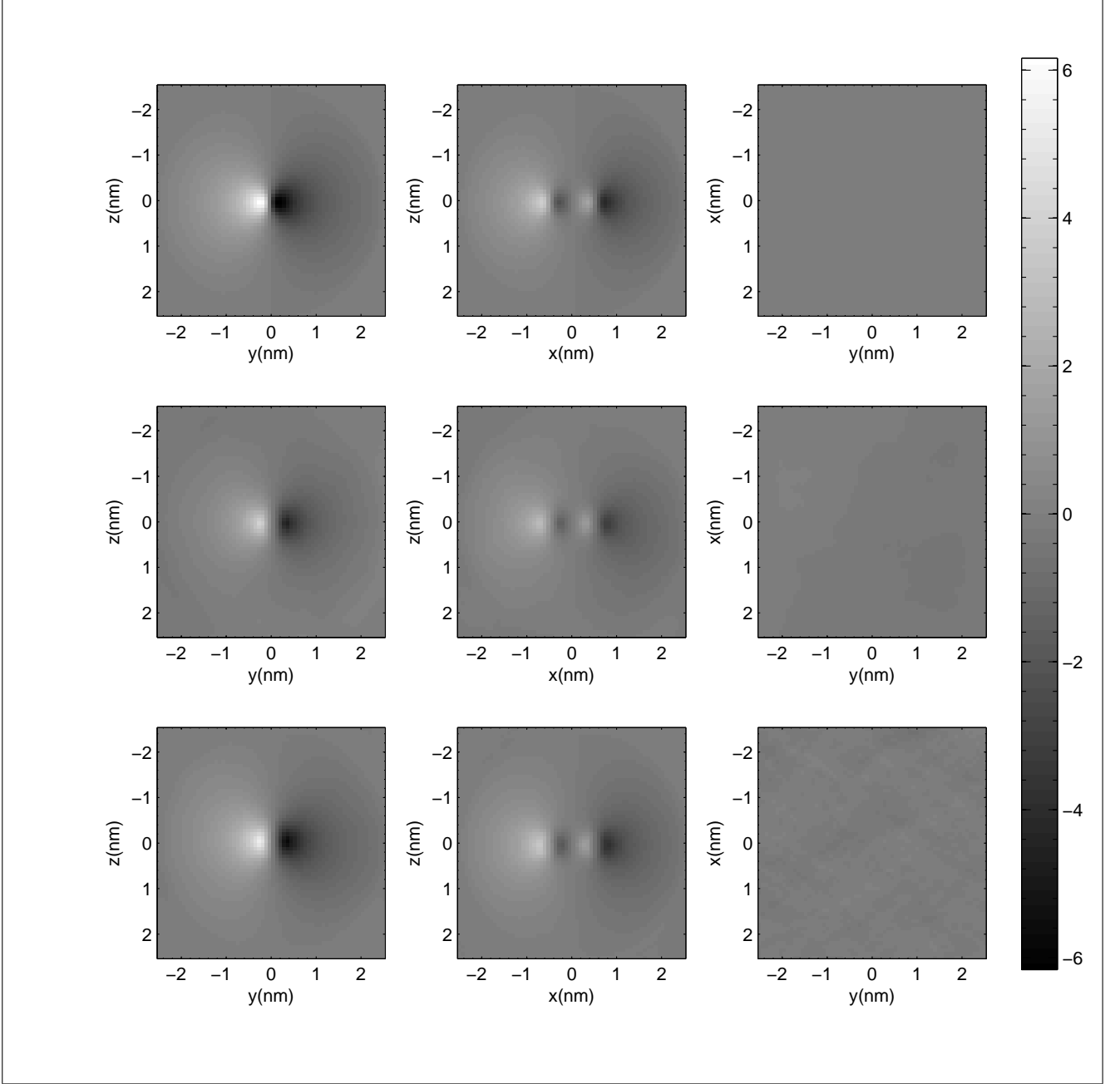
Figure 14: Projections of the simulated exact and reconstructed vector potentials for two parallel dipoles separated by 1 nm in the x direction with 4% Poisson noise in the simulated micrographs. Each dipole has magnetic moment μ, such that $\mu\Delta = 12 \times \frac{\hbar}{e} \times 10^6$ Am^3. Top row: Projections of exact vector potential. Middle row: phase maps reconstructed from the simulated micrographs. Bottom row: Projections of the vector potential reconstructed from the phase maps using filtered back-projection. The columns show projections in the x, y, and z directions respectively. The normalised RMS error in the reconstruction of the vector potential for this case was 22%. The grayscale indicates the phase at the image plane in radians.
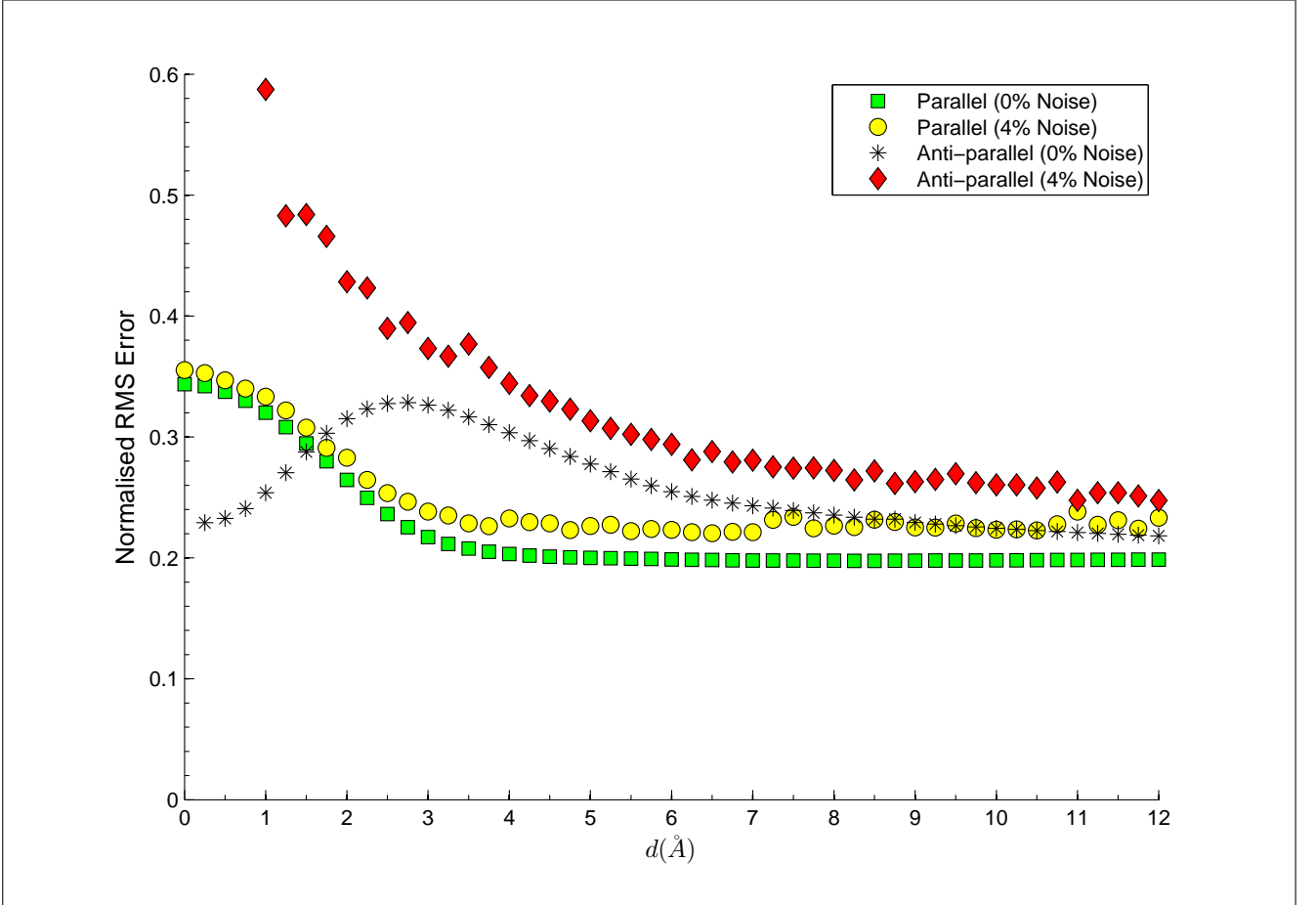
Figure 15: RMS error versus separation for two dipoles with $\mu\Delta = 7.91 \times 10^{-6}$ Am^3. For the case of antiparallel dipoles, the magnetic moments are $\mu\hat{\mathbf{z}}$ and $-\mu\hat{\mathbf{z}}$, respectively, and for the case of parallel dipoles, both have magnetic moment $\mu\hat{\mathbf{z}}$. The separation d is in the x-direction with the origin being the midpoint between the two dipoles.
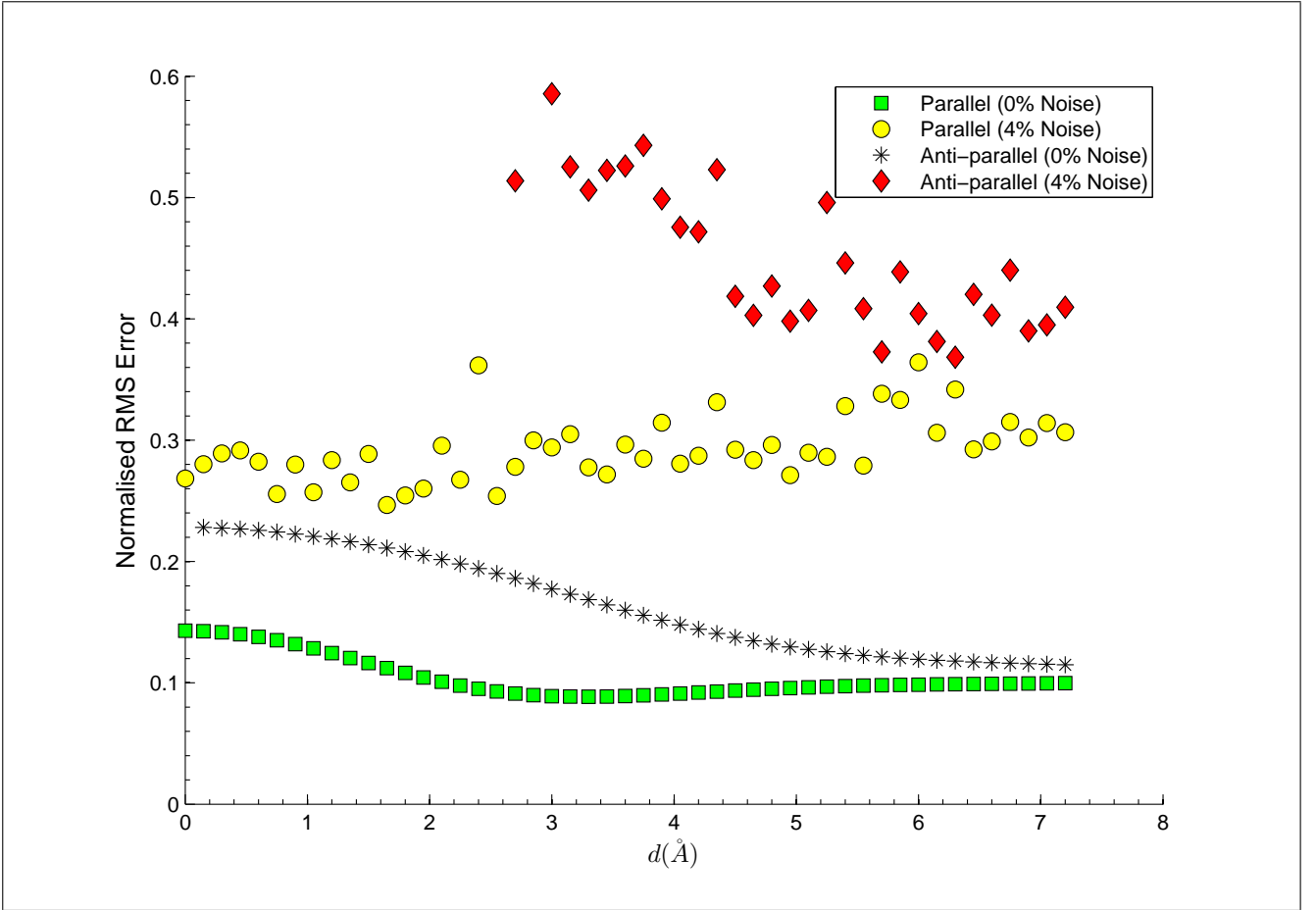
Figure 16: RMS error versus separation for two dipoles with a magnetic moment of magnitude μ such that $\mu\Delta = 2.85 \times 10^{-6}$ Am^3. All aspects of the simulations, except for the value of $\mu\Delta$, were identical to those used for figure 15.

6.3 Limitations of the Dipole Model

The simulations involving the reconstruction of the dipole vector potential discussed in the preceding subsections have a major drawback. In order to avoid instability arising from the singularity in the vector potential (Eq. (32)) at the origin, a regularisation parameter δ has been employed. The choice of δ is somewhat arbitrary, and as its value is increased, the reconstruction becomes more accurate. But the larger the value of δ, the less accurately the computed vector potential models the vector potential of an ideal dipole. Because of this, the calculated RMS errors cannot be assumed to be the values that would arise in an experimental application of these techniques.

In order to avoid this problem, geometries for which the vector potential contains no singularities were used in subsequent simulations.

6.4 Uniformly Magnetised Spheres

The magnetised sphere is an object of interest in the field of nanomagnetism [53], [15], [54], with particular relevance to biomedicine and biotechnology [55]. The uniformly magnetised sphere is a good model for realistic magnetic nanospheres [53], so simulations using this geometry will provide useful data to enable accurate characterisation of these objects. The vector potential

of a uniformly magnetised sphere is given by [34:200]

$$\mathbf{A} = \frac{4\pi}{3} M_0 a^2 \left(\frac{r_<}{r_>^2} \right) \begin{bmatrix} -y/r \\ x/r \\ 0 \end{bmatrix}, \tag{39}$$

where m_0 is the magnetisation, a is the radius of the sphere, and $r_<$ is the smaller and $r_>$ the larger of a and r. For $r > a$, this reduces to the ideal dipole vector potential given by Eq. (32). Inside the sphere ($r < a$) the vector potential is proportional to r and the singularity at the origin, present in the dipole vector potential, is avoided.

The analysis of the effects of noise and defocus on the RMS error reported in section 6.1 were repeated using the model of the uniformly magnetised sphere. A surface plot showing the RMS error as a function of $M_0\Delta$ and σ is shown in figure 17, and log-log plots showing the relationship between Δ_{opt} and σ, and E_{min} and σ, are shown in figure 18(a) and 18(b), respectively[6]. Linear regression was applied to the data and, for the relationship $\Delta_{opt} = A_3\sigma^{p_3}$, the slope and intercept of the log-log plot were found to be $p_3 = 0.48 \pm 0.05$ and $\ln(A_3) = 3.74 \pm 0.05$, respectively. For the relationship $E_{min} - C = A_4\sigma^{p_4}$, the slope and intercept of the log-log plot were $p_4 = 0.83 \pm 0.02$ and $\ln(A_4) = -3.58 \pm 0.02$. This results in the equations:

$$\Delta_{opt} = (42 \pm 2) \times \sigma^{(0.48\pm0.05)} \tag{40}$$

and

$$E_{min} = (28 \pm 1) \times \sigma^{0.83} \times 10^{-3} + 0.065 \tag{41}$$

The powers, p_3 and p_4, were consistent with those (p_1 and p_2) from section 6.1, but p_3 was inconsistent with the cube-root law discussed in that section. Future work should include an analytical derivation of these relationships against which the above results can be compared.

---

[6]The exit phase is proportional to the magnetisation of the sphere, so the defocus and magnetisation have been expressed as the product, $M_0\Delta$, analogous to the product, $\mu\Delta$, used in section 6.1
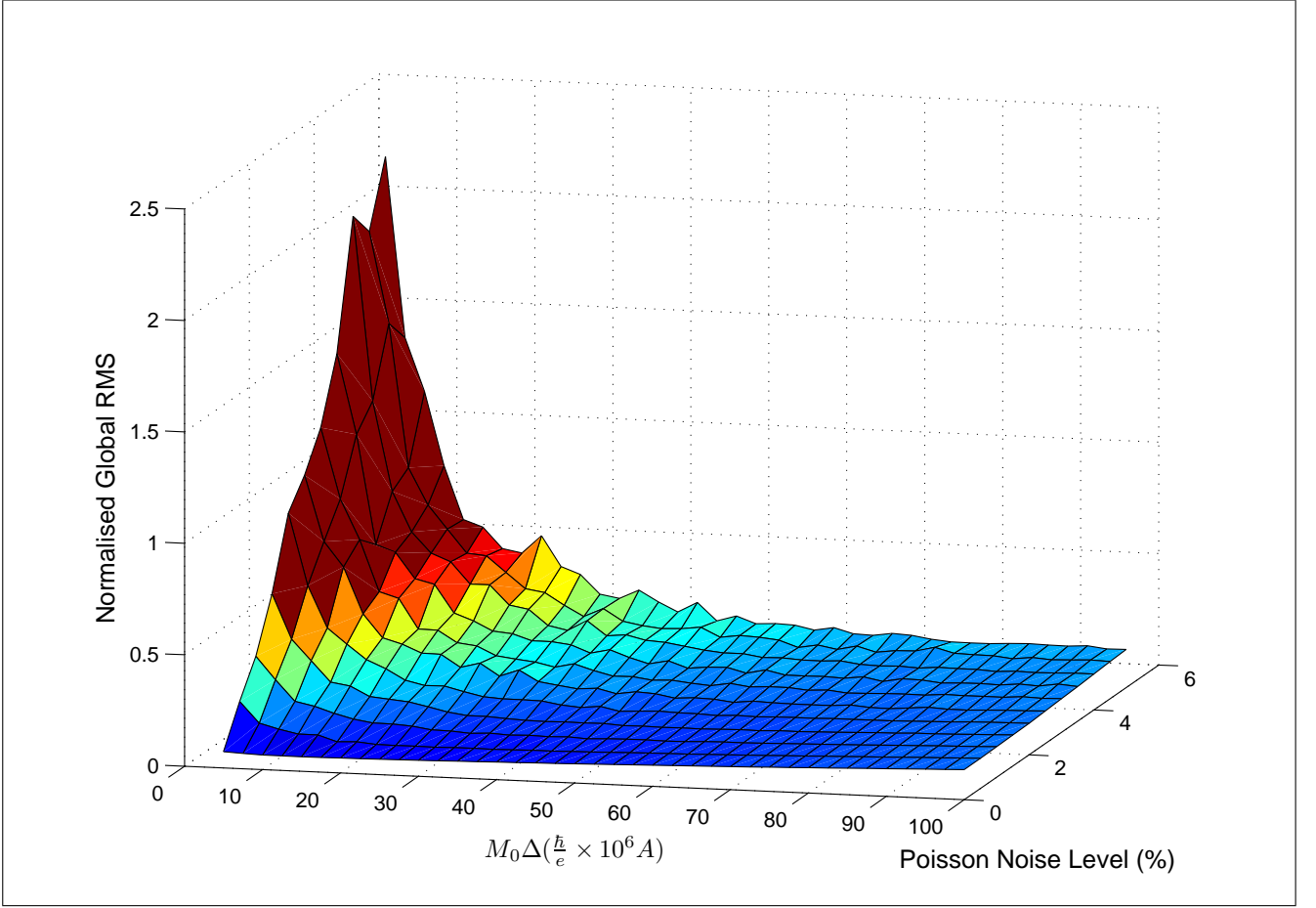
Figure 17: Plot of reconstruction error against noise level and the product of the magnetisation M_0 and the defocus Δ for a uniformly magnetised sphere of radius 0.4 nm centred at the origin.
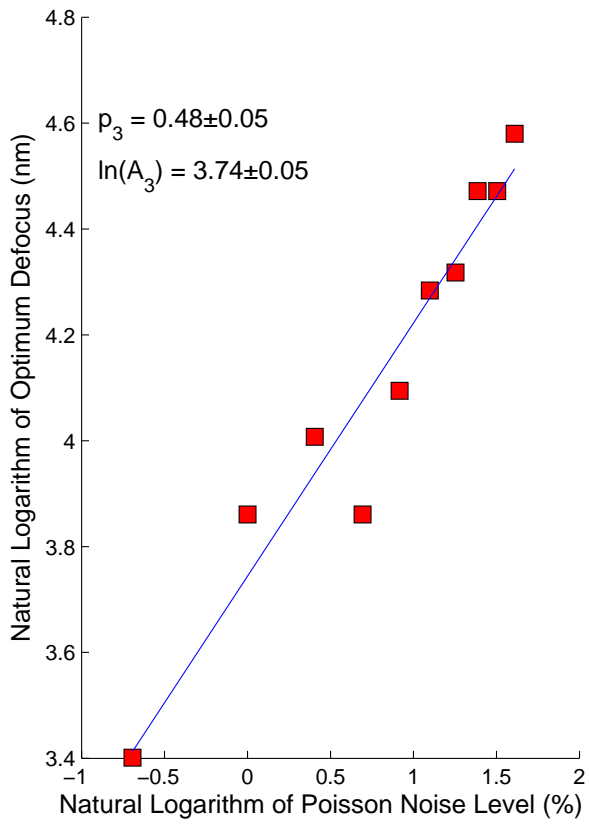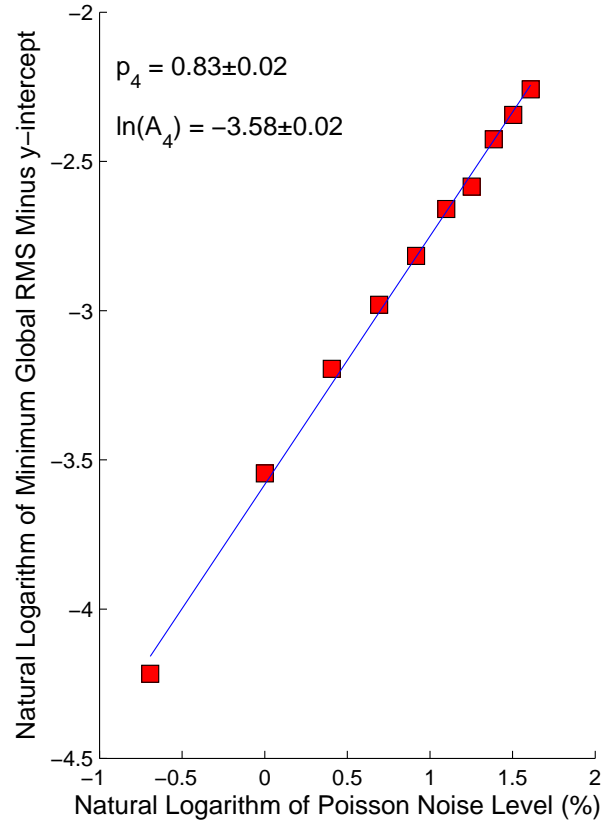
Figure 18: Properties of the reconstruction of the vector potential of a uniformly magnetised sphere. (a) The natural logarithm of optimum defocus plotted against the natural logarithm of noise level. (b) The natural logarithm of the minimum error (minus the noise-free error) plotted against the natural logarithm of noise level.
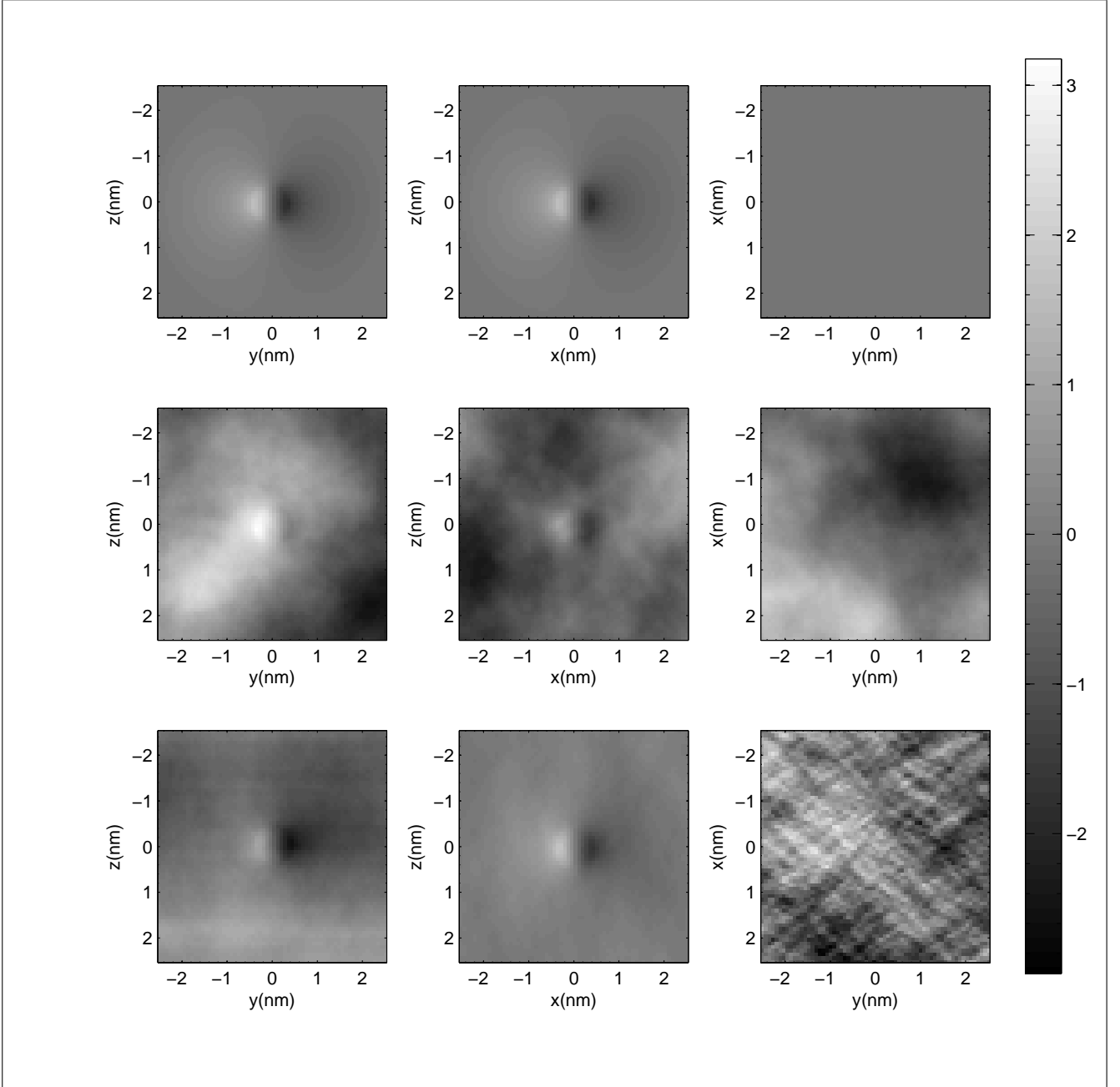
Figure 19: Projections of the simulated exact and reconstructed vector potentials for a uniformly magnetised sphere of radius $R = 0.4$ nm and magnetisation and defocus such that $M_0\Delta = 5 \times \frac{\hbar}{e} \times 10^6$ A. Top row: Projections of exact vector potential. Middle row: phase maps reconstructed from the simulated micrographs with 5% noise. Bottom row: Projections of the vector potential reconstructed from the phase maps using filtered back-projection. The columns show projections in the x, y, and z directions respectively. The RMS error in the reconstruction of the vector potential for this case was 224%.

6.5 Regularisation of the TIE

To avoid instabilities in the TIE algorithm a regularisation parameter α has been employed. (See Eq. (14)). A small value of $\alpha/a = 1/1280 \equiv \alpha_0/a$ (where a is the width of the Fourier transformed phase map in units of m^{-1}) was chosen for the simulations discussed in the preceding subsections. This value permitted accurate reconstructions under certain circumstances, i.e., for certain choices of noise-level and defocus, so it was used without further justification. In order to allow for more appropriate choices of α in future work, simulations were performed on the uniformly magnetised sphere of the previous subsection, with σ, Δ, and α varied over successive simulations. For each value of σ and Δ, an optimum value of α (α_{opt}) that minimised the RMS error in the reconstructed vector potential was found. Figure 20 shows a surface plot of α_{opt}/a versus σ and Δ.

An important feature to note is that the optimum defocus for a given noise level (calculated using Eq. (37) and shown in blue on the xy plane) produces a small value of α_{opt}. Heuristically, this is not unexpected. The errors caused by the TIE algorithm are due to the errors in the approximation of $\partial I/\partial z$ - both from noise in the micrographs and errors caused by the finite difference approximation to the derivative - being amplified by the singularity. Therefore, minimizing the errors in $\partial I/\partial z$, by choosing an appropriate defocus, should allow for less drastic regularisation, and this is supported by the simulated data. These results lend support to the choice of $\alpha = \alpha_0$ used for the previous simulations. In addition to this, it should give one confidence in future applications that a small choice for α is appropriate when $\Delta \approx \Delta_{opt}$.

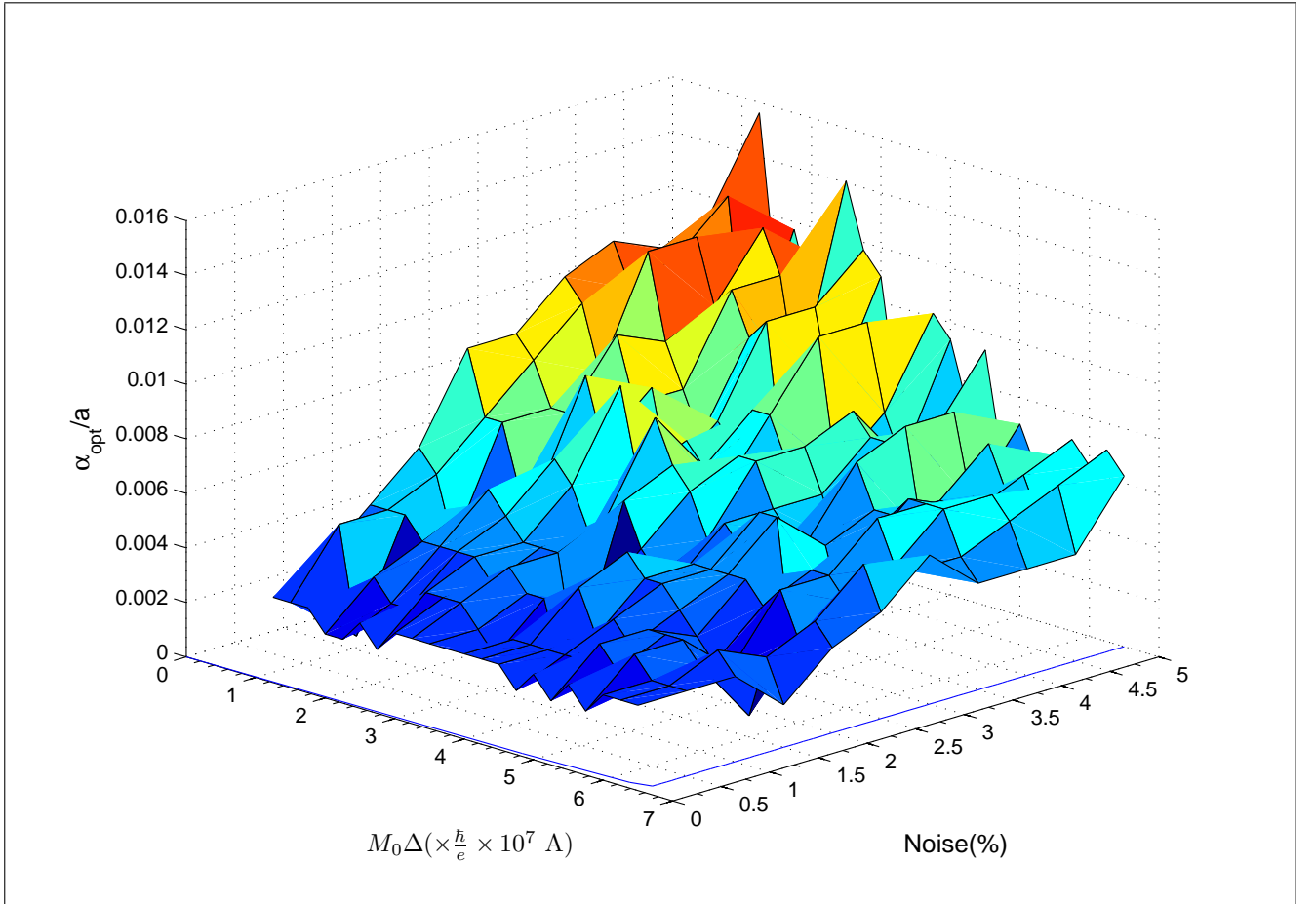
Figure 20: Plot showing the optimum choice of α (α_{opt}) as a function of $M_0\Delta$ and σ. The blue line on the xy plane gives the optimum $M_0\Delta$ for a given noise level within the range of values used for the plot.

Under some experimental circumstances, using the optimum defocus may not be practical and the value of α should be increased to account for this. Figure 21 shows a wireframe plot of reconstruction errors for $\alpha = \alpha_0$ as a function of $M_0\Delta$ and σ (taken from figure 17), and the grayscale surface showing the errors for $\alpha = \alpha_{opt}$ as a function of $M_0\Delta$ and σ.
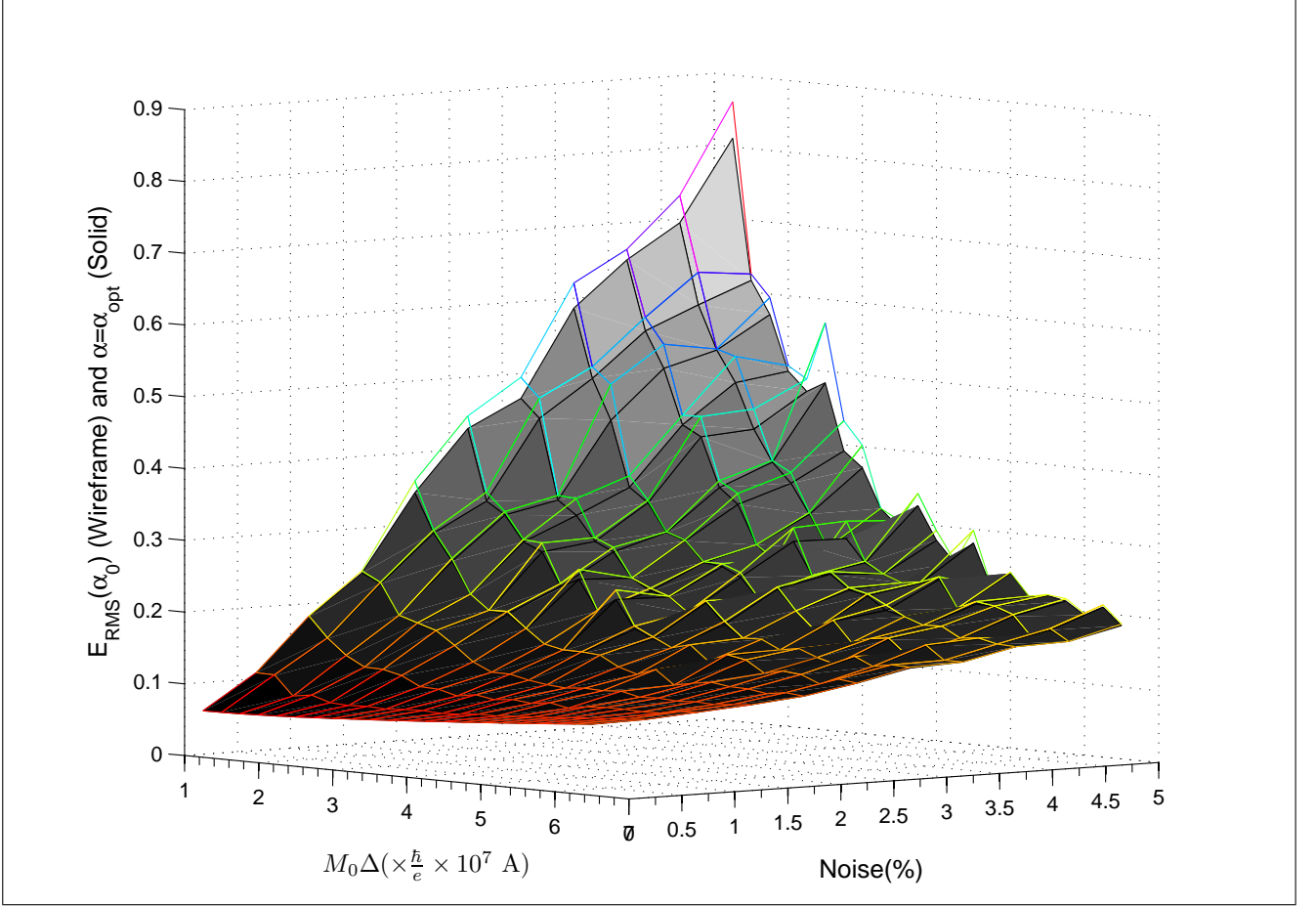

Figure 21: Reproduction of part of the surface of figure 17 (here shown in wireframe), with the corresponding surface showing E_{RMS} versus $M_0\Delta$ when $\alpha = \alpha_{opt}$.

The errors are noticibly reduced in the high noise, small defocus region when α_{opt} is used rather than α. This is expected because, from figure 20, α_{opt} is much larger in this region, so the choice of $\alpha = \alpha_0$ is not as effective. Determining α_{opt} for a given task may be simplified by noting that its value can be determined to some degree of accuracy by estimating the normalised RMS error in the reconstruction when $\alpha = \alpha_0$ (This will be referred to as $E_{RMS}(\alpha_0)$). Figure 22 shows a plot of $\ln(\alpha_{opt}/a)$ versus $\ln(E_RMS(\alpha_0))$ for several values of $M_0\Delta$, though a much larger set of data (25 different defoci in total) were used to obtain the line of best fit and its slope, p_3, and intercept, $\ln(A_3)$. Linear regression was also applied to each set of points corresponding to a single defocus to obtain their own best fit lines (not shown). The slope and intercept of these lines were plotted against $M_0\Delta$ (figures 23(a) and 23(b), respectively). The slope of figure 23(a) was determined to be 0.1 ± 0.6, so it is consistent with the slopes in figure 22 being independent of defocus (and magnetisation).
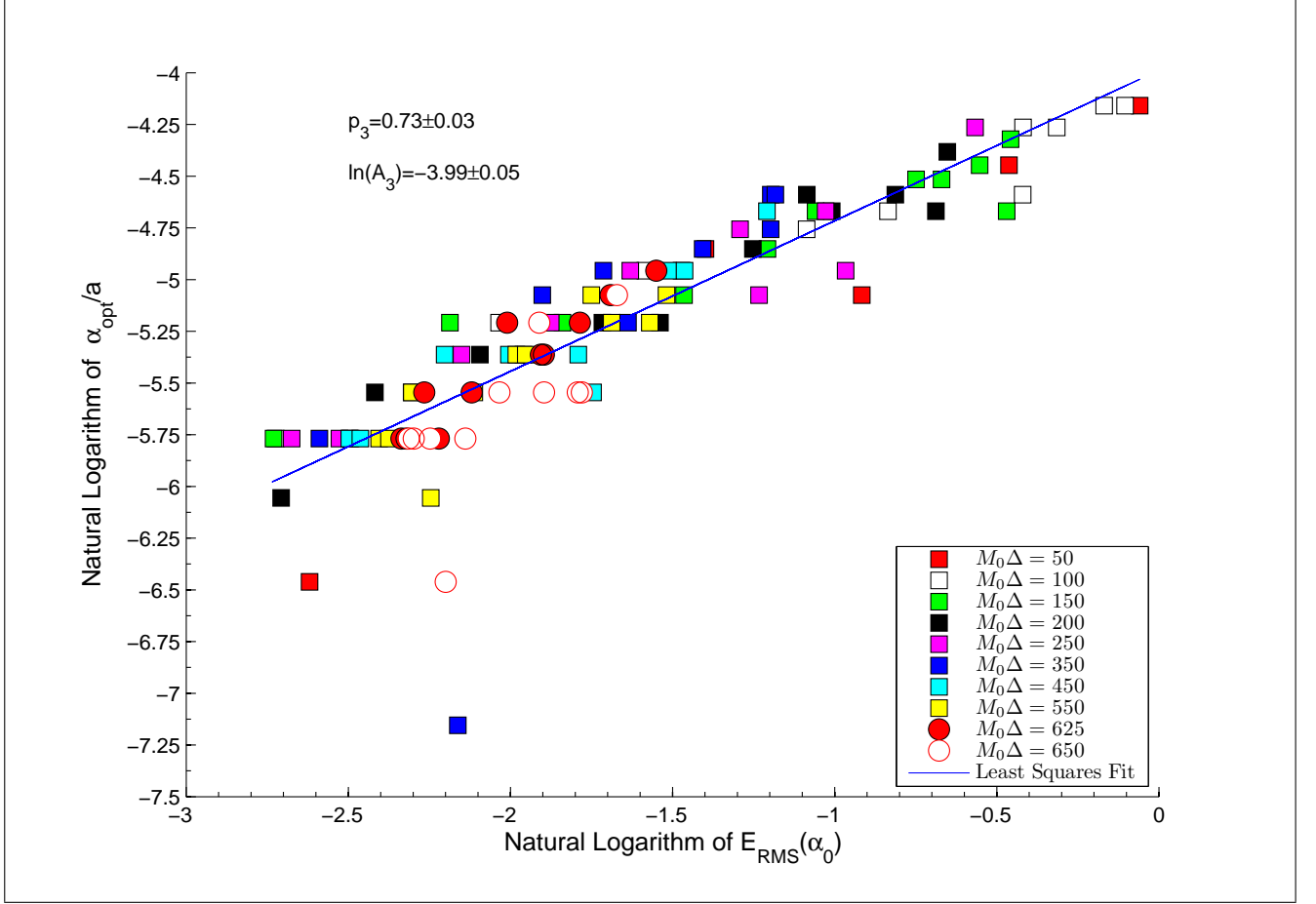
Figure 22: Relationship between α_{opt}/a and $E_{RMS}(\alpha_0)$ for $\alpha_0/a = 1/1280$, linearised by assuming a power law and plotting the natural logarithm of both quantities. The line of best fit and its associated slope, p_3, and intercept, $\ln(A_3)$, were calculated using data for all values of $M_0\Delta$ between 50 and 650 in increments of 25, but only a subset of these are shown on the plot. $M_0\Delta$ is given in units of $\hbar/e \times 10^5$ A.

Figure 23: Relationship between (a) the slope, and (b) the intercept, of the best fit line of α_{opt} versus $E_{RMS}(\alpha_0)$ as a function of $M_0\Delta$, showing little or no correlation.

7 Further Research

The simulations performed for this project involved the modeling of simple magnetic structures, namely single dipoles, pairs of dipoles, and single magnetised spheres. A more comprehensive study would require the modeling of more complicated geometries for which the accuracy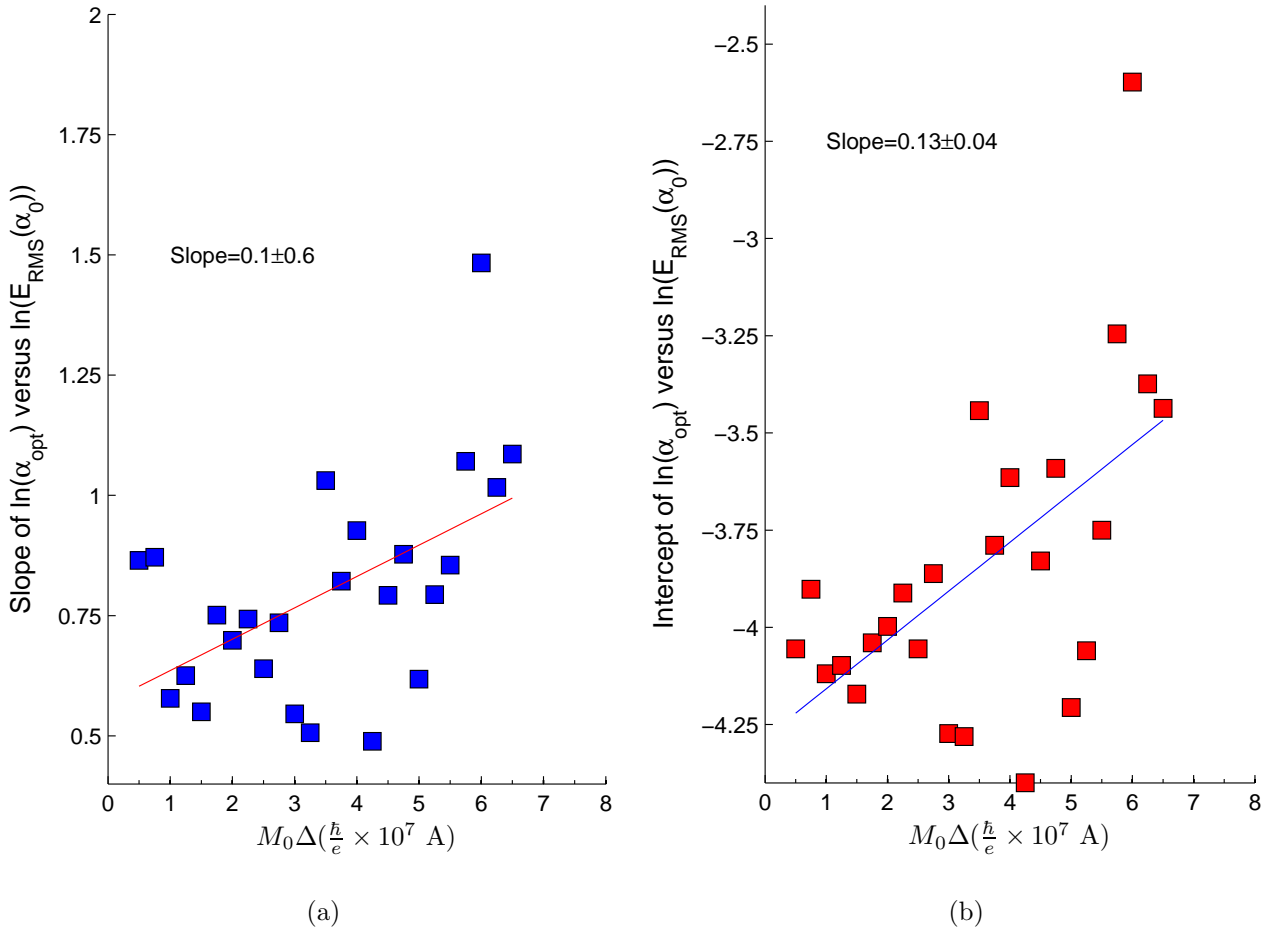 of these methods could be determined. The possibilities for choosing a form of the vector potential are limitless, but because these techniques will be used to visualise real-world magnetic nanostructures, it makes sense to perform simulations that model these objects. In this project, the modeling of nanospheres has been performed, but without concern for a realistic length scale. Appropriate scaling would provide a more realistic predicted error for a given noise level. In addition to nanospheres, other nanostructures of interest include, nanocubes [56], skyrmions [57], and current distributions [58]. Any of these can be arranged in arrays to provide a more complicated vector potential under which the behaviour of the reconstruction algorithms can be examined. For any chosen geometry, the behaviour of the algorithms under different conditions will be examined. In the remainder of this section, several specific avenues of investigation are proposed.

7.1 Tilt Range and Tilt Resolution

In practice, a tilt series is usually not taken over a full 180° range due to design limitations of the sample holder [37:105-107]. This will cause missing information in the projections, leading to errors in the reconstructed potentials. An analysis of how the RMS error varies with tilt range can be performed using simulations like those used in this project. This would provide a minimum tilt range to avoid unacceptably large error.

In addition to the tilt range, the tilt resolution - the number of tilt angles per degree - will contribute to the amount of information acquired, and hence to the RMS error in the reconstruction. Every simulation in the current work utilised 100 tilt angles over a range of 180°, so the tilt resolution was about 0.56 images/degree. The reconstructions presented in this report incurred a non-zero error in the absence of noise, and the limited tilt resolution may be responsible for some of this error. Future simulations will involve increased tilt resolution to ascertain whether the errors can be significantly improved by increasing the number of images in each tilt series.

7.2 Incorporating Scalar Potentials

The work carried out for this project has focused solely on the magnetic vector potential. In practice, however, samples will have an electric scalar potential in addition to the magnetic vector potential. Separation of these two contributions to the total phase shift by flipping the sample as discussed in section 3.3 can cause errors in the reconstruction due to misalignment when flipping the sample. This was noted as a cause of errors in the work carried out by Phatak et al. [6] (discussed in section 4). The errors caused by misalignment could be quantified by simulating both vector and scalar potentials, and comparing the RMS error of the reconstructed potentials against misalignment angle for various angles. Other parameters, such as noise level and defocus distance, could also be varied in the reconstructions to determine whether the errors due to misalignment depend on them.

Given a relationship between misalignment angle and RMS error for various geometries and parameter values, for subsequent experiments one could estimate an upper bound on the allowable angle of misalignment in order to prevent the RMS error rising above an unacceptable value. It is expected that the more quickly varying the vector field over space, the lower the tolerance to misalignment because the errors in the projections will be higher and these errors propagate to the total RMS error after tomographic reconstruction.

7.3 Electron Beam Attenuation

The objects modelled in this project have all been pure phase objects. That is, the phase of the electron beam is modified as it passes through the sample, but the total flux recorded at the detector remains the same (ignoring uncertainties in the electron count due to shot noise) regardless of whether the beam passes through the sample or not. This is not the case in general, as absorption will cause attenuation of the beam as it traverses the sample resulting in a non-uniform intensity across the image plane. Thus, the TIE method used must be in the form of Eq. (12). A thorough analysis of errors will need to take this effect into account by modelling the attenuation caused by interactions with the sample. This would be particularly appropriate for modelling structures such as the nanoparticles discussed at the beginning of this section.

7.4 Multiple Defoci

The use of multiple images at different defocus distances in phase contrast imaging has been investigated with promising results [59], [60], but the work on VFET to date has used, for each tilt angle, only one underfocus, one overfocus, and one in-focus image. There are different ways to implement multiple defocus distances. The defocus images can be used in higher order approximations to the spatial derivative along the direction of propagation of the electron beam, providing a more accurate approximation to the phase shift [59]. Alternatively, two different phase maps can be retrieved using a small defocus for one and a large defocus for the other [50]. The phase map obtained using large defocus modified by a low pass filter can be combined with that obtained using small defocus, modified by a high pass filter.

Taking multiple defocus images will incur a cost in terms of acquisition time, and this must be taken into account when determining the usefulness of such a technique. When comparing methods that use different numbers of defocus images, those using fewer images should be simulated with a lower level of noise in the micrographs, according to Eq. 22, to account for this difference in acquisition time. The methods can then be compared in terms of how the reconstruction error varies with total acquisition time.

7.5 Regularisation of Singularities in the Reconstruction Algorithm

In the simulations used for this project, solutions at singular surfaces in the reconstruction formulae have been made finite by linear interpolation of $\tilde{\mathbf{A}}$ at the singular surfaces. While this prevents a division by zero at the singular surface, it does so without considering the instability at nearby pixels, so noise in the phase maps is magnified near the singular surfaces, contributing to the overall error in the reconstruction. Regularisation of the algorithm using a smooth band-stop filter such as that given by Eq. (29) is expected to be more effective in minimising the errors than the interpolation used for this project. The effect of a particular choice of the bandwidth, ω, should be examined, and its optimum value could be determined as a function of other parameters, analogous to the work performed on the TIE regularisation parameter, α, for the current project.

7.6 Effect of Resolution in the Micrographs on the Reconstruction

The work carried out for this project involved the simulation of micrographs on a 128×128 pixel grid. The CCDs commonly used in transmission electron microscopy are capable of much higher resolution: up to 4000×4000 pixels [49:120]. Increased resolution can improve the accuracy of the reconstruction simply by providing a more detailed picture of the exit phase, as well as the reconstructed potentials. However, the projection approximation has been employed in expressing the phase maps as line integrals along the direction of electron beam propagation. At high resolution the projection approximation breaks down [61], and this will cause errors when these phase maps are used to reconstruct the vector potential. These considerations imply that, given a specific geometry and set of parameters, there will be an optimum resolution below which the errors due to the discrete representation of the continuous quantities (the intensity and phase of the electron wavefield at the detector, and the magnetic vector potential) dominate, and above which errors due to the break down of the projection approximation dominate. If the low resolution reconstruction was compared against a low resolution exact vector potential, it may appear that using a single voxel would be the most accurate approach if it gives an RMS error of nearly zero, but this is clearly absurd. In order to meaningfully evaluate the RMS error

in this context, a low voxel number grid containing a reconstructed vector potential must be converted to a high voxel number grid via subdivision of each voxel, and *then* compared against the exact vector potential at high resolution. This comparison is a more meaningful measure of how effectively a lower resolution reconstruction can approximate the real (continuous) vector potentials than is achieved by comparing the low resolution reconstruction to a low resolution exact vector potential.

Because of the number of computational operations involved in the volumetric reconstruction of vector fields, performing the process at high-resolution will be time-consuming and the viability will depend on the processing power of available computers. A comparison of reconstructions at various resolutions could be performed to assess the gain in terms of accuracy, and the cost in processing time, as the resolution increases. Because the FFT is utilised in processing the images, the phase retrieval and tomographic reconstruction will be fastest when the number of pixels per row and per column are powers of two. To investigate the effect of intermediate resolutions, zero-padding can be used to increase the actual dimensions of the image to a power of two. For example, a 100×100 pixel image could be padded with zeros to produce a 128×128 pixel image.

7.7   Analytical Models

The work presented in this thesis was performed using computer simulations of the VFET process. Where analytical models for relationships (such as that between optimum defocus and noise level) have been presented, the justification has been solely based on heuristic grounds. This has included visual inspection of plotted data, as well as the drawing of analogies with previous, related work. Future work on this topic should include a rigorous analytical derivation of the power laws obtained in section 6.1, as well as relationships involving the TIE regularisation parameter α, such as that betwen α_{opt} and $E_{RMS}(\alpha_0)$, obtained using simulations and reported in section 6.5.

8   Conclusions

Using computer simulations of a magnetic dipole and a uniformly magnetised sphere, the relationship between optimum defocus and noise level was found to be consistent with a power law. For the case of the dipole, this was consistent with the analytical result, a cube root law, obtained by Paganin et al. [50] for the TIE phase retrieval process. For the uniformly magnetised sphere, the exponent was not consistent with the analytical result. For both geometries, the results obtained in this work were mutually consistent within the uncertainties derived from the spread of the data. The relationship between minimum error and noise level was consistent with a power law plus a constant (the error in the reconstruction when no noise is present in the micrographs). There is currently no theoretical basis for this power law. Future work will involve deriving an analytical form of the relationship between minimum error and noise level, and optimum defocus and noise level, that includes the effects of tomography, and comparing these with the numerical results.

Curves were obtained, using simulations, that show how the reconstruction error changes as a function of separation distance, for both parallel and antiparallel dipoles, in the presence and absence of noise. The errors increase with decreasing separation (except for the case of antiparallel dipoles with no noise) and this places limits on the resolving capability of the reconstruction algorithm. For antiparallel dipoles, the net vector potential decreases with

decreasing separation distance, and this causes the reconstruction to be unstable in the presence of noise at short separation distances. This effect has significance in terms of the accuracy of the reconstruction at, for example, magnetic domain boundaries.

Regularisation of the TIE (Eq. (14)) was investigated. Approximate values for the optimum regularisation parameter, α_{opt}, were obtained, as a function of noise level and defocus, using simulations. It was found that the value of α_{opt} increased as the errors due to changing defocus and noise increased. A power law relationship between α_{opt} and the normalised global RMS error in the reconstruction using a small regularisation parameter, α_0 was found. This relationship showed little or no dependence on the defocus distance used, indicating that the increase in α_{opt} improves the reconstruction error due to errors in the phase maps, without regard for whether those errors are caused by noise or a poor choice of defocus.

Future work will include the analytical derivation of the power laws mentioned above, as well as more sophisticated numerical simulations, exploring aspects of the reconstruction process not covered in the current work, such as: varying tilt range, separating magnetic and electric components of the phase shift, modeling objects that are not pure phase, and using multiple defoci for the phase retrieval.

References

[1] R. Zehbe, A. Haibel, H. Riesemeier, U. Gross, C. J. Kirkpatrick, H. Schubert, and C. Brochhausen, "Going beyond histology. Synchrotron micro-computed tomography as a methodology for biological tissue characterization: from tissue morphology to individual cells," *J. Roy. Soc. Interface*, vol. 7, no. 42, pp. 49–59, 2010.

[2] G. Y. Fan, S. J. Young, P. Miller, and M. H. Ellisman, "Conditions for electron tomographic data-acquisition," *J. Electron Microsc.*, vol. 44, no. 1, pp. 15–21, 1995.

[3] M. Richards, J. Budaj, M. Agafonov, and O. Sharova, "Applications of doppler tomography in 2D and 3D," in *Binaries - Key to Comprehension of the Universe* (Prsa, A and Zejda, M, ed.), vol. 435 of *Astr. Soc. P.*, pp. 77–80, Astronomical soc pacific, 2010.

[4] S. J. Norton, "Unique tomographic reconstruction of vector fields using boundary data," *IEEE Trans. Image Process.*, vol. 1, no. 3, pp. 406–412, 1992.

[5] T. Jansson, M. Almqvist, K. Strahlen, R. Eriksson, G. Sparr, H. Persson, and K. Lindstrom, "Ultrasound Doppler vector tomography measurements of directional blood flow," *Ultrasound Med. Biol.*, vol. 23, no. 1, pp. 47–57, 1997.

[6] C. Phatak, A. K. Petford-Long, and M. De Graef, "Three-dimensional study of the vector potential of magnetic structures," *Phys. Rev. Lett.*, vol. 104, no. 25, 253901, 2010.

[7] C. Phatak, M. Beleggia, and M. De Graef, "Vector field electron tomography of magnetic materials: Theoretical development," *Ultramicroscopy*, vol. 108, no. 6, pp. 503–513, 2008.

[8] R. Bracewell, ed., *The Fourier Transform and its Applications*. third ed., 2000.

[9] R. P. Yu, M. J. Morgan, and D. M. Paganin, "Lorentz-electron vector tomography using two and three orthogonal tilt series," *Phys. Rev. A*, vol. 83, no. 2, 023813, 2011.

[10] T. M. Buzug, *Computed Tomography: From Photon Statistics to Modern Cone-beam CT*. Springer, 2008.

[11] F. Accaino, G. Bohm, G. Dal Moro, G. Madrussani, G. Rossi, and A. Vesnaver, "The use of 4D seismic for ocean acoustic tomography," in *Theoretical and Computational Acoustics 2001* (Shang, EC and Li, Q and Gao, TF, ed.), pp. 219–225, 2002.

[12] M. Sawicki, W. Stefanowicz, and A. Ney, "Sensitive SQUID magnetometry for studying nanomagnetism," *Semicond. Sci. Technol.*, vol. 26, no. 6, SI, 2011.

[13] J. Iqbal, X. Liu, A. Majid, and R. Yu, "Synthesis and physical properties of Mn doped ZnO dilute magnetic semiconductor nanostructures," *J. Supercond. Nov. Magn.*, vol. 24, no. 5, pp. 699–704, 2011.

[14] P. A. Midgley and R. E. Dunin-Borkowski, "Electron tomography and holography in materials science," *Nat. Mater.*, vol. 8, no. 4, pp. 271–280, 2009.

[15] S. Wu, W. Jiang, Z. Sun, J. Dai, L. Liu, and F. Li, "Preparation of novel magnetic fluorescent nanospheres by sonochemical method," *J. Magn. Magn. Mater.*, vol. 323, no. 16, pp. 2170–2173, 2011.

[16] S. Bamrungsap, J. A. Phillips, X. Xiong, Y. Kim, H. Wang, H. Liu, A. Hebard, and W. Tan, "Magnetically driven single DNA nanomotor," *Small*, vol. 7, no. 5, pp. 601–605, 2011.

[17] J. M. Teixeira, R. Lusche, J. Ventura, R. Fermento, F. Carpinteiro, J. P. Araujo, J. B. Sousa, S. Cardoso, and P. P. Freitas, "Versatile, high sensitivity, and automatized angular dependent vectorial Kerr magnetometer for the analysis of nanostructured materials," *Rev. Sci. Instrum.*, vol. 82, no. 4, 2011.

[18] K. Bennemann, "Magnetic nanostructures," in *Physical Properties of Nanosystems*, Nato security through science series B: Physics and biophysics, pp. 215–232, 2011.

[19] J. I. Martin, J. Nogues, K. Liu, J. L. Vicent, and I. K. Schuller, "Ordered magnetic nanostructures: fabrication and properties," *J. Magn. Magn. Mater.*, vol. 256, no. 1-3, pp. 449–501, 2003.

[20] L. Reimer and H. Kohl, *Transmission Electron Microscopy: Physics of Image Formation.* Springer, fifth ed., 2008.

[21] L. J. Allen, H. M. L. Faulkner, M. P. Oxley, and D. Paganin, "Phase retrieval and aberration correction in the presence of vortices in high-resolution transmission electron microscopy," *Ultramicroscopy*, vol. 88, no. 2, pp. 85 – 97, 2001.

[22] C. Dorrer and J. D. Zuegel, "Optical testing using the transport-of-intensity equation," *Opt. Express*, vol. 15, no. 12, pp. 7165–7175, 2007.

[23] S. Bajt, A. Barty, K. A. Nugent, M. McCartney, M. Wall, and D. Paganin, "Quantitative phase-sensitive imaging in a transmission electron microscope," *Ultramicroscopy*, vol. 83, no. 1-2, pp. 67–73, 2000.

[24] A. Tonomura, "Applications of electron holography," *Rev. Mod. Phys.*, vol. 59, no. 3, Part 1, pp. 639–669, 1987.

[25] E. Voelkl, L. F. Allard, and B. Frost, "Electron holography: Recent developments," *Scanning Microscopy*, vol. 11, pp. 407–416, 1997.

[26] Y. Aharonov and D. Bohm, "Significance of electromagnetic potentials in the quantum theory," *Phys. Rev.*, vol. 115, no. 3, pp. 485–491, 1959.

[27] H. Cheng, H. Liu, Q. Zhang, and S. Wei, "Phase retrieval using the transport-of-intensity equation," in *Fifth International Conference on Image and Graphics.*, pp. 417 –421, 2009.

[28] L. J. Allen and M. P. Oxley, "Phase retrieval from series of images obtained by defocus variation," *Opt. Commun.*, vol. 199, no. 1-4, pp. 65 – 75, 2001.

[29] T. E. Gureyev, A. Roberts, and K. A. Nugent, "Partially coherent fields, the transport-of-intensity equation, and phase uniqueness," *J. Opt. Soc. Am. A*, vol. 12, no. 9, pp. 1942–1946, 1995.

[30] C. Dorrer and J. D. Zuegel, "Optical testing using the transport-of-intensity equation," *Opt. Express*, vol. 15, no. 12, pp. 7165–7175, 2007.

[31] L. Waller, Y. Luo, S. Y. Yang, and G. Barbastathis, "Transport of intensity phase imaging in a volume holographic microscope," *Opt. Lett.*, vol. 35, no. 17, pp. 2961–2963, 2010.

[32] D. Paganin and A. Nugent, "Noninterferometric phase determination," in *Adv. Imag. Elect. Phys.*, vol. 118, pp. 85–127, Academic Press, 2001.

[33] W. O. Saxton, *Computer Techniques for Image Processing in Electron Microscopy.* Academic Press, 1978.

[34] J. D. Jackson, *Classical Electrodynamics.* John Wiley & Sons, Inc., third ed., 1999.

[35] S. J. Lade, D. Paganin, and M. J. Morgan, "Electron tomography of electromagnetic fields, potentials and sources," *Opt. Commun.*, vol. 253, no. 4-6, pp. 392–400, 2005.

[36] A. Kingston and I. Svalbe, "Projective transforms on periodic discrete image arrays," vol. 139 of *Adv. Imag. Elect. Phys*, pp. 75–177, 2006.

[37] C. Phatak, *On the use of phase reconstructed vector field electron tomography for the 3-D study of magnetic materials.* Ph.D. thesis, University of Calgary, Canada, 2000.

[38] S. J. Lade, D. Paganin, and M. J. Morgan, "3-D Vector tomography of Doppler-transformed fields by filtered-backprojection," *Opt. Commun.*, vol. 253, no. 4-6, pp. 382–391, 2005.

[39] C. Slump and H. Ferwerda, "Statistical aspects of image handling in low-dose electron microscopy of biological material," in *Adv. Electon. El. Phys.*, vol. 66, pp. 201–308, Academic Press, 1986.

[40] J. C. Russ, *The Image Processing Handbook.* CRC Press, fifth ed., 2007.

[41] J. S. Silva, A. Silva, and B. S. Santos, "Image denoising methods for tumor discrimination in high-resolution computed tomography," *J. Digit. Imaging*, vol. 24, no. 3, pp. 464–469, 2011.

[42] S. Kret, P. Ruterana, A. Rosenauer, and D. Gerthsen, "Extracting quantitative information from high resolution electron microscopy," *Phys. Status Solidi B*, vol. 227, no. 1, pp. 247–295, 2001.

[43] E. R. Mcveigh, R. M. Henkelman, and M. J. Bronskill, "Noise and filtration in magnetic-resonance imaging," *Med. Phys.*, vol. 12, no. 5, pp. 586–591, 1985.

[44] F. Q. Ye, J. A. Frank, D. R. Weinberger, and A. C. McLaughlin, "Noise reduction in 3D perfusion imaging by attenuating the static signal in arterial spin tagging (ASSIST)," *Magn. Res. Med.*, vol. 44, no. 1, pp. 92–100, 2000.

[45] K. Kitamura, H. Iida, M. Shidahara, S. Miura, and I. Kanno, "Noise reduction in pet attenuation correction using non-linear gaussian filters," *IEEE T. Nucl. Sci.*, vol. 47, no. 3, pp. 994 –999, 2000.

[46] A. S. Frangakis and R. Hegerl, "Noise reduction in electron tomographic reconstructions using nonlinear anisotropic diffusion," *J. Struct. Biol.*, vol. 135, no. 3, pp. 239 – 250, 2001.

[47] W. Press, S. Teukolsky, W. Vetterling, and B. Flannery, *Numerical Recipes in C: The Art of Scientific Computing.* second ed., 1997.

[48] M. De Graef, *Introduction to Conventional Transmission Electron Microscopy.* Cambridge University Press, 2003.

[49] D. Williams and C. Carter, *Transmission Electron Microscopy: A textbook for Materials Science.* Springer Science, second ed., 2009.

[50] D. Paganin, A. Barty, P. McMahon, and K. Nugent, "Quantitative phase-amplitude microscopy. III. The effects of noise," *J. Microsc-Oxford*, vol. 214, pp. 51–61, 2004.

[51] J. R. Taylor, *An Introduction to Error Analysis.* University Science Books, second ed., 1997.

[52] B. D. Arhatari, W. P. Gates, N. Eshtiaghi, and A. G. Peele, "Phase retrieval tomography in the presence of noise," *J. Appl. Phys.*, vol. 107, no. 3, 2010.

[53] X. Liu, Y. Guan, Z. Ma, and H. Liu, "Surface modification and characterization of magnetic polymer nanospheres prepared by miniemulsion polymerization," *Langmuir*, vol. 20, no. 23, pp. 10278–10282, 2004.

[54] H. Xu, N. Tong, L. Cui, Y. Lu, and H. Gu, "Preparation of hydrophilic magnetic nanospheres with high saturation magnetization," *J. Magn. Magn. Mater.*, vol. 311, no. 1, pp. 125–130, 2007.

[55] Y. Tai, L. Wang, G. Fan, J.-m. Gao, H. Yu, and L. Zhang, "Recent research progress on the preparation and application of magnetic nanospheres," *Polym. Int.*, vol. 60, no. 7, pp. 976–994, 2011.

[56] L. Wang, X. Wang, J. Luo, B. N. Wanjala, C. Wang, N. A. Chernova, M. H. Engelhard, Y. Liu, I.-T. Bae, and C.-J. Zhong, "Core-shell-structured magnetic ternary nanocubes," *J. Am. Chem. Soc.*, vol. 132, no. 50, pp. 17686–17689, 2010.

[57] X. Z. Yu, Y. Onose, N. Kanazawa, J. Park, J. H. Han, Y. Matsui, N. Nagaosa, and Y. Tokura, "Real-space observation of a two-dimensional skyrmion crystal," *Nature*, vol. 465, no. 7300, pp. 901–904, 2010.

[58] S. McVitie and G. White, "Imaging amperian currents by Lorentz microscopy," *J. Phys. D-Appl. Phys.*, vol. 37, no. 2, pp. 280–288, 2004.

[59] L. Waller, L. Tian, and G. Barbastathis, "Transport of Intensity phase-amplitude imaging with higher order intensity derivatives," *Opt. Express*, vol. 18, no. 12, pp. 12552–12560, 2010.

[60] M. Soto and E. Acosta, "Improved phase imaging from intensity measurements in multiple planes," *Appl. Optics*, vol. 46, no. 33, pp. 7978–7981, 2007.

[61] H. Cohen, M. Schmid, and W. Chiu, "Estimates of validity of projection approximation for 3-dimensional reconstructions at high-resolution," *Ultramicroscopy*, vol. 14, no. 3, pp. 219–226, 1984.